

The reach of next-to-leading-order perturbation theory for the matter bispectrum

Davit Alkhanishvili,¹ Cristiano Porciani,¹ Emiliano Sefusatti,^{2,3,4} Matteo Biagetti,^{2,3,4,5} Andrei Lazanu,⁶ Andrea Oddo,^{3,5} and Victoria Yankelevich⁷

¹*Argelander Institut für Astronomie der Universität Bonn, Auf dem Hügel 71, 53121 Bonn, Germany*

²*Istituto Nazionale di Astrofisica, Osservatorio Astronomico di Trieste, via Tiepolo 11, 34143 Trieste, Italy*

³*Institute for Fundamental Physics of the Universe, via Beirut 2, 34151 Trieste, Italy*

⁴*Istituto Nazionale di Fisica Nucleare, Sezione di Trieste, Via Valerio 2, 34127 Trieste, Italy*

⁵*SISSA - International School for Advanced Studies, Via Bonomea 265, 34136 Trieste, Italy*

⁶*Laboratoire de Physique de l'École normale supérieure, ENS, Université PSL, CNRS, Sorbonne Université, Université de Paris, F-75005 Paris, France*

⁷*Astrophysics Research Institute, Liverpool John Moores University, Liverpool, L3 5RF, UK*

Accepted XXX. Received YYY; in original form ZZZ

ABSTRACT

We provide a comparison between the matter bispectrum derived with different flavours of perturbation theory at next-to-leading order and measurements from an unprecedentedly large suite of N -body simulations. We use the χ^2 goodness-of-fit test to determine the range of accuracy of the models as a function of the volume covered by subsets of the simulations. We find that models based on the effective-field-theory (EFT) approach have the largest reach, standard perturbation theory has the shortest, and ‘classical’ resummed schemes lie in between. The gain from EFT, however, is less than in previous studies. We show that the estimated range of accuracy of the EFT predictions is heavily influenced by the procedure adopted to fit the amplitude of the counterterms. For the volumes probed by galaxy redshift surveys, our results indicate that it is advantageous to set three counterterms of the EFT bispectrum to zero and measure the fourth from the power spectrum. We also find that large fluctuations in the estimated reach occur between different realisations. We conclude that it is difficult to unequivocally define a range of accuracy for the models containing free parameters. Finally, we approximately account for systematic effects introduced by the N -body technique either in terms of a scale- and shape-dependent bias or by boosting the statistical error bars of the measurements (as routinely done in the literature). We find that the latter approach artificially inflates the reach of EFT models due to the presence of tunable parameters.

Key words: cosmology: large-scale structure of Universe – theory – methods: statistical

1 INTRODUCTION

The three-point correlation function or its Fourier counterpart, the bispectrum, are the lowest-order clustering statistics that characterise departures from Gaussianity in the galaxy distribution. Although these statistics have a long history dating back to the earliest galaxy redshift surveys (Peebles & Groth 1975; Gaztanaga 1994; Scoccimarro et al. 2001; Verde et al. 2002; Gaztañaga et al. 2005; Pan & Szapudi 2005; Kulkarni et al. 2007; McBride et al. 2011; Gil-Marín et al. 2015a,b, 2017; Slepian et al. 2017a,b, 2018; Pearson & Samushia 2018; Gualdi et al. 2019), their importance has always been rather marginal. On the contrary, they are expected to play a key role to fully exploit the potential of forthcoming observations such as those conducted with the Dark-Energy Spectroscopic Instrument (DESI, DESI Collaboration et al. 2016) and the Euclid satellite (Laureijs et al. 2011) by improving the estimation of cos-

mological parameters and breaking degeneracies that emerge from the analysis of the power spectrum (e.g. Yankelevich & Porciani 2019; Chudaykin & Ivanov 2019; Heinrich & Doré 2020; Barreira 2020; Gualdi & Verde 2020; Moradinezhad Dizgah et al. 2021; Eggemeier et al. 2021; Hahn & Villaescusa-Navarro 2021; Agarwal et al. 2021; Samushia et al. 2021).

In order to achieve this goal, it is crucial that accurate theoretical models are available in the mildly non-linear regime of perturbation growth. The information we want to retrieve, in fact, is distributed over many triangular configurations the number of which grows rapidly with the minimum considered length scale (Sefusatti & Scoccimarro 2005; Sefusatti et al. 2006; Chan & Blot 2017). Therefore, an essential feature of the models is that they give accurate predictions over the widest possible range of scales. In this paper, we investigate the accuracy of perturbative models for the bispectrum of the matter density field against large suites of

N -body simulations. This way we test the primary building block of models for the galaxy bispectrum that should also address additional sources of non-linearities (e.g. galaxy biasing, redshift-space distortions) and discreteness effects.

Standard perturbation theory (SPT, see [Bernardeau et al. 2002](#), for a review) has long been the workhorse for theoretical predictions on clustering statistics in cosmology. Based on the so-called single-stream approximation (in which velocity dispersion is neglected), it expands the fluid equations for a self-gravitating pressureless fluid in terms of the linear density contrast and velocity potential. The evolution of the bispectrum generated from Gaussian initial conditions to the lowest non-vanishing order in SPT was pioneered by [Fry \(1984\)](#). Next-to-leading-order (NLO) corrections were then discussed in [Scoccimarro \(1997\)](#) and [Scoccimarro et al. \(1998\)](#). Over the years, alternative schemes have been developed to model the growth of cosmological perturbations and the calculation of the matter bispectrum has been combined with techniques that resum infinite subsets of perturbative contributions in both the Eulerian ([Crocce & Scoccimarro 2006a,b](#); [Bernardeau et al. 2008, 2012](#); [Crocce et al. 2012](#)) and the Lagrangian descriptions ([Matsubara 2008](#); [Rampf & Wong 2012](#)). More recently, following a general trend in theoretical physics, an effective field theory (EFT) that approximately describes gravitational instability on ‘perturbative’ scales and averages over small-scale fluctuations provided a new framework to model the matter bispectrum ([Angulo et al. 2015](#); [Baldauf et al. 2015c](#)). In this case, feedback from the small scales to the large scales is expressed in terms of a number of parameters that are fit to observational data or numerical simulations. This construction appears to be successful in extending the range of accuracy of the models. In this work, we compare the different approaches ranging from SPT to EFT with two large suites of N -body simulations. Since many of the forthcoming observational probes will concentrate on intermediate redshifts, we only consider data at redshift $z = 1$.

Although several authors already tried to determine the domain of accuracy (sometimes dubbed the reach or k -reach) of different perturbative predictions for the bispectrum (e.g. [Angulo et al. 2015](#); [Baldauf et al. 2015b](#); [Lazanu et al. 2016](#); [Steele & Baldauf 2021](#)), our work critically evidences that the results depend on a number of factors that have been rarely explored in depth. In the first place, they depend on the overall volume covered by the N -body simulations which determines the size of the statistical uncertainty affecting the measurements. Besides, when these random errors are small, estimates of the reach are influenced by systematic shifts due to imperfections of the N -body technique (which are not easy to model and to account for). Furthermore, in the case of the EFT, on top of the sheer goodness-of-fit criterion one should also consider the consistency (as a function of the minimum length scale under study) of the best-fitting values for the parameters that determine the amplitude of the EFT corrections. In addition, the number of free parameters and the range of scales used in the fitting procedure might influence the inferred range of accuracy. By considering all these effects, we provide a much more comprehensive investigation of the reach of perturbative models for the matter bispectrum at NLO than what is already available in the literature. As a byproduct of our study, we also obtain analogous results for the matter power spectrum which we use in order to calibrate the EFT corrections for the bispectrum.

This paper is organized as follows. In section 2, we briefly review the PT models we use while, in section 3, we introduce the simulation suites and the bispectrum measurements. In section 4, we describe how the perturbative models are implemented in practice

and how we use the χ^2 goodness-of-fit test to determine their range of accuracy. Our results are presented and critically discussed in section 5. Finally, we summarise our findings in section 6.

2 PERTURBATION THEORY

Given the Fourier transform of the mass-density contrast at redshift z , $\delta(\mathbf{k}, z)$, the matter power spectrum, $P(k, z)$, and the bispectrum, $B(\mathbf{k}_1, \mathbf{k}_2, \mathbf{k}_3, z)$, can be defined in terms of the two- and three-point equal-time correlators as

$$\langle \delta(\mathbf{k}_1, z) \delta(\mathbf{k}_2, z) \rangle = (2\pi)^3 \delta_{\text{D}}(\mathbf{k}_{12}) P(k_1, z), \quad (1)$$

and

$$\langle \delta(\mathbf{k}_1, z) \delta(\mathbf{k}_2, z) \delta(\mathbf{k}_3, z) \rangle = (2\pi)^3 \delta_{\text{D}}(\mathbf{k}_{123}) B(\mathbf{k}_1, \mathbf{k}_2, \mathbf{k}_3, z), \quad (2)$$

where the angle brackets denote averaging over an ensemble of realisations, δ_{D} is the Dirac delta function, and $\mathbf{k}_{i\dots j} \equiv \mathbf{k}_i + \dots + \mathbf{k}_j$. In this section, we briefly review a number of perturbative methods that have been used to model $P(k, z)$ and $B(\mathbf{k}_1, \mathbf{k}_2, \mathbf{k}_3, z)$ on quasi-linear scales and that we will test against numerical simulations.

2.1 Standard perturbation theory

In the standard model of cosmology, the formation of the large-scale structure of the Universe is dominated by a dark-matter component. Although the physical origin of dark matter is still unclear, it is generally assumed that, on macroscopic scales, it can be modelled as a self-gravitating medium governed by the collisionless Boltzmann (or Vlasov) equation in a cosmological background. The Vlasov-Poisson system can be written as a hierarchy of coupled evolution equations for the velocity moments of the phase-space distribution function (the so-called macroscopic transport equations).

SPT assumes that the dark matter can be treated as a pressureless ideal fluid governed by the continuity, Euler, and Poisson equations. These are obtained by setting to zero the second velocity moment of the phase-space distribution function and thus correspond to considering the so-called ‘single-stream’ regime in which there is a well defined velocity everywhere.

By considering irrotational flows only, the dynamic equations are written in terms of two scalar fields, namely the matter-density contrast and the divergence of the peculiar velocity. The solution of the linearised transport equations is $\delta^{(1)}(\mathbf{k}, z) \equiv D(z) \delta_{\text{L}}(\mathbf{k})$ where $D(z)$ denotes the linear growth factor and $\delta_{\text{L}}(\mathbf{k})$ is the linear solution at the time in which $D = 1$. Following an established practice, we set $D = 1$ at the present time, corresponding to $z = 0$.

The fastest growing solution for $\delta(\mathbf{k}, z)$ is written as an expansion in terms of the linear density contrast. In particular, if we consider the Einstein-de Sitter (EdS) cosmological model, it follows that

$$\delta(\mathbf{k}, z) = \sum_{n=1}^{\infty} [D(z)]^n \delta^{(n)}(\mathbf{k}), \quad (3)$$

with

$$\delta^{(n)}(\mathbf{k}) = \int \frac{d^3\mathbf{k}_1 \dots d^3\mathbf{k}_n}{(2\pi)^{3(n-1)}} \delta_{\text{D}}(\mathbf{k} - \mathbf{k}_{1\dots n}) F_n(\mathbf{k}_1, \dots, \mathbf{k}_n) \times \delta_{\text{L}}(\mathbf{k}_1) \dots \delta_{\text{L}}(\mathbf{k}_n), \quad (4)$$

where the (symmetrised) kernels F_n describe the gravitational coupling between Fourier modes of the linear solution and can be obtained by recursion relations ([Goroff et al. 1986](#)).

Once the statistical properties of $\delta_L(\mathbf{k})$ have been specified, the expressions above allow us to derive perturbative expansions for the power spectrum and the bispectrum of the matter density contrast. These are conveniently computed by following a diagrammatic approach which is analogous to the Feynman diagrams in quantum electrodynamics (e.g. [Bernardeau et al. 2002](#)). We classify as ‘tree-level’ all terms associated with tree diagrams (in the sense of graph theory) and as ‘loop corrections’ those associated with diagrams containing n -loops (and that require n three-dimensional integrations).

Under the assumption that $\delta_L(\mathbf{k})$ is a Gaussian random field, the leading-order term for $P(k, z)$ coincides with the linear power spectrum, $P_{\text{SPT}}^{\text{tree}}(k, z) = [D(z)]^2 P_L(k)$, where $\langle \delta_L(\mathbf{k}) \delta_L(\mathbf{k}') \rangle = (2\pi)^3 \delta_D(\mathbf{k} + \mathbf{k}') P_L(k)$, while, for the bispectrum, we have

$$B_{\text{SPT}}^{\text{tree}}(\mathbf{k}_1, \mathbf{k}_2, \mathbf{k}_3, z) = 2 [D(z)]^4 F_2(\mathbf{k}_1, \mathbf{k}_2) P_L(k_1) P_L(k_2) + 2 \text{ perms.} \quad (5)$$

Accounting for the NLO corrections, we obtain

$$P_{\text{SPT}}(k, z) \simeq P_{\text{SPT}}^{\text{tree}}(k, z) + P_{\text{SPT}}^{1\text{-loop}}(k, z), \quad (6)$$

$$B_{\text{SPT}}(\mathbf{k}_1, \mathbf{k}_2, \mathbf{k}_3, z) \simeq B_{\text{SPT}}^{\text{tree}}(\mathbf{k}_1, \mathbf{k}_2, \mathbf{k}_3, z) + B_{\text{SPT}}^{1\text{-loop}}(\mathbf{k}_1, \mathbf{k}_2, \mathbf{k}_3, z). \quad (7)$$

Their explicit expressions are given in Appendix A.

On large scales and at early times, tree-level SPT provides an accurate description of both the matter power spectrum and bispectrum. At late times, however, one-loop corrections over-predict P on mildly non-linear scales ($k \sim 0.1 h \text{ Mpc}^{-1}$, [Crocce & Scoccimarro 2006a](#); [Carlson et al. 2009](#); [Taruya et al. 2009](#)) and higher-order terms do not improve the quality of the predictions (e.g. [Blas et al. 2014](#)). The reason for the breakdown of SPT is well understood: loop integrals extend to scales at which the assumptions of the theory do not apply (e.g. due to the generation of vorticity and velocity dispersion at orbit crossing, [Pueblas & Scoccimarro 2009](#)) and physics becomes non-perturbative. The failure of SPT on small scales thus corrupts its predictions for the large scales.

2.2 Renormalised perturbation theory

Higher-order SPT corrections in the expansions for the matter power spectrum and the bispectrum may have larger amplitudes than lower-order ones. In other words, increasing the order of the expansions does not necessarily improve their accuracy ([Crocce & Scoccimarro 2006a](#); [Blas et al. 2014](#)). Renormalised perturbation theory (RPT, [Crocce & Scoccimarro 2006a,b, 2008](#); [Bernardeau et al. 2008, 2012](#); [Crocce et al. 2012](#)) forms one of the first attempts to overcome the shortcomings of SPT (for an approach based on the renormalisation group see [Matarrese & Pietroni 2007](#); [Pietroni 2008](#)). In RPT, infinite subsets of SPT diagrams are resummed and organized in terms of multi-point propagators defined as the ensemble average of the infinitesimal variation of the evolved cosmic fields with respect to the linear solutions (see Appendix B). A key property is that all the statistical quantities such as the power spectra and the bispectra can be expressed in terms of the multi-point propagators. This is known as the multi-point-propagator expansion or Γ -expansion.

RPT has two main advantages over SPT. First, all the contributions to the power spectrum are positive and adding higher-order terms improves the range of accuracy of the theory as no cancellations occur between successive loop corrections. Second, the

exponential factor appearing in the high- k limit of the multi-point propagators effectively damps the contributions to the loop integrals outside the range of validity of the expansion, thus preventing some of the issues which occur in SPT.

One can construct a matching scheme for any multi-point propagator which smoothly interpolates between the resummed behaviour in the high- k limit and the SPT results at low k ([Bernardeau et al. 2012](#); [Crocce et al. 2012](#); [Taruya et al. 2012](#)). In this paper, we adopt the form derived in [Taruya et al. \(2012\)](#) which is known as regularised PT (REGPT). An alternative matching scheme (dubbed $\text{MPT}_{\text{BREEZE}}$) has been proposed by [Crocce et al. \(2012\)](#) and implemented for the bispectrum in [Lazanu et al. \(2016\)](#). We have verified that REGPT and $\text{MPT}_{\text{BREEZE}}$ give nearly identical results and, for this reason, there is no point in considering both here.

2.3 Lagrangian perturbation theory

In the Lagrangian approach to fluid dynamics, the trajectories of the fluid elements are characterized in terms of the displacement field $\Psi(\mathbf{p}, t)$ which links the Lagrangian position \mathbf{p} and the Eulerian position \mathbf{x} (at time t) through the relation $\mathbf{x}(\mathbf{p}, t) = \mathbf{p} + \Psi(\mathbf{p}, t)$. Lagrangian perturbation theory (LPT) is derived by using $\Psi(\mathbf{p}, t)$ as a perturbative variable (e.g. [Zel’dovich 1970](#); [Moutarde et al. 1991](#); [Catelan 1995](#)). In this framework, the Eulerian matter density can be expressed as

$$\delta(\mathbf{k}) = \int d^3 \mathbf{p} e^{-i\mathbf{k} \cdot \mathbf{p}} \left[e^{-i\mathbf{k} \cdot \Psi(\mathbf{p})} - 1 \right], \quad (8)$$

(where we do not write the time dependence explicitly to simplify notation) which allows us to write an expression for the power spectrum

$$P(\mathbf{k}) = \int d^3 \Delta_{12} e^{-i\mathbf{k} \cdot \Delta_{12}} \left[\langle e^{-i\mathbf{k} \cdot [\Psi(\mathbf{p}_1) - \Psi(\mathbf{p}_2)]} \rangle - 1 \right], \quad (9)$$

and the bispectrum

$$B(\mathbf{k}_1, \mathbf{k}_2, \mathbf{k}_3) = \int d^3 \Delta_{12} \int d^3 \Delta_{13} e^{-i\mathbf{k} \cdot (\Delta_{12} + \Delta_{13})} \times \left[\langle e^{-i\mathbf{k}_2 \cdot [\Psi(\mathbf{p}_1) - \Psi(\mathbf{p}_2)] - i\mathbf{k}_3 \cdot [\Psi(\mathbf{p}_1) - \Psi(\mathbf{p}_3)]} \rangle - 1 \right], \quad (10)$$

where $\Delta_{ij} \equiv \mathbf{p}_i - \mathbf{p}_j$, and the expectation value only depends on the separation Δ_{12}, Δ_{13} due to homogeneity ([Taylor & Hamilton 1996](#); [Fisher & Nusser 1996](#); [Matsubara 2008](#); [Rampf & Wong 2012](#)). A perturbative expansion of equations (9) and (10) can then be obtained by means of the cumulant expansion theorem

$$\langle e^{-iX} \rangle = \exp \left[\sum_{N=1}^{\infty} \frac{(-i)^N}{N!} \langle X^N \rangle_c \right], \quad (11)$$

where $\langle X^N \rangle_c$ represents the N^{th} order cumulant of the random variable X . Expanding the powers of X with the binomial theorem, two types of terms are obtained: those depending on Ψ at one point, and those depending on Ψ at multiple points. It turns out that, if both sets of terms are expanded to the same perturbative order, the ‘classical’ LPT results coincide with the SPT expressions for both the power spectrum and the bispectrum ([Matsubara 2008](#); [Rampf & Wong 2012](#)).

2.4 Resummed Lagrangian perturbation theory

On closer inspection, it emerges the classical LPT predictions for P and B can be improved by reorganising the perturbative expansion.

The key issue is that, for large Lagrangian separations, the terms depending on Ψ at one point are much larger than those depending on Ψ at multiple points. It thus makes sense to keep the first set of terms inside the argument of the exponential and use the cumulant expansion only for the second set (Matsubara 2008; Rampf & Wong 2012). This approach is generally referred to as resummed Lagrangian perturbation theory (RLPT) as it corresponds to a partial resummation of the perturbative expansion¹. The resulting formulae for calculating P and B to NLO are presented in Appendix C. In Lazanu et al. (2016), it has been shown that the RLPT predictions are similar to those of MPTBREEZE.

2.5 Effective Field Theory of Large-Scale Structure

Effective theories have become a widely used tool in modern physics. In a system characterised by a wide range of scales, they isolate a set of degrees of freedom and describe them with a simplified model without having to deal with the complex (and often unknown) underlying dynamics. The impact of the physics one wishes to neglect on the degrees of freedom one desires to study is computed as a perturbation theory in terms of one or more expansion parameters.

The effective field theory of large-scale structure (EFT, Baumann et al. 2012; Carrasco et al. 2012, 2014a,b; Hertzberg 2014; Porto et al. 2014; Senatore & Zaldarriaga 2015) attempts to provide an effective description of the long-wavelength modes of the matter density field by integrating out (i.e. averaging over) the short-wavelength ones. Contrary to the models introduced in the previous sections, the EFT does not rely on the single-stream approximation and considers an effective stress tensor which is expressed in terms of all operators of the long-wavelength density and velocity fields (and their derivatives) allowed by the symmetries of the problem: the equivalence principle along with the assumption of statistical isotropy and homogeneity. The effective stress tensor is Taylor expanded in the long-wavelength fluctuations giving rise to an infinite series of unknown parameters each associated with a perturbative order. These parameters can be treated as coupling constants in the Wilsonian approach to renormalisation. We can imagine that the theory contains a cutoff (i.e. the loop corrections are integrated up to a maximum wavenumber) and the couplings of the effective theory can be changed to enforce that the physics at low k is always the same when the cutoff is changed. Therefore, the parameters of the effective theory fulfil two purposes. In the EFT expressions for observables, they generate ‘counterterms’ which can be used to cancel out the UV sensitivity of the loop integrals in SPT (i.e. their dependence on the cutoff scale). This can be done order by order in perturbation theory. Moreover, the remaining cutoff-independent part of the counterterms should actually quantify the impact of the non-perturbative physics on the long-wavelength modes by introducing new ‘effective’ interactions among long-wavelength modes. The amplitude of this part, however, cannot be derived from the EFT (which is blind to small-scale physics) and must be fixed empirically by comparison with numerical simulations or marginalised over in the analysis of actual observational data (see, e.g. Ivanov et al. 2020; d’Amico et al. 2020).

EFT assumes the existence of a scale, generally indicated in terms of the wavenumber k_{NL} , around which physics becomes non-perturbative and the effective description becomes meaningless.

¹ Note that RLPT is different from the so-called convolution Lagrangian perturbation theory (e.g. Carlson et al. 2013) which further extends the partial resummation but has not yet been applied to the bispectrum.

Several lines of reasoning suggest that the derivative expansion of the long-wavelength fields can be organised so that the expansion parameter of the perturbation theory is k/k_{NL} , meaning that more and more terms should be considered to get accurate expressions for the correlators of the matter field as k approaches k_{NL} .

The fact that perturbations of all wavelengths (barring virialised structures) evolve on similar time scales constitutes a complication of the theory. It follows from this that the EFT is non-local in time, i.e. the long-wavelength perturbations depend on the entire past history of the short-wavelength modes. This is difficult to treat and, in practical applications, the local-in-time approximation is almost invariably invoked. We adopt the same strategy in our study. In particular, we focus on the specific parameterisation of the counterterms appearing in the one-loop expressions for the matter power spectrum and bispectrum presented in Angulo et al. (2015). Considering the linear Taylor approximation of the effective stress tensor in the long-wavelength perturbations gives the EFT power spectrum to NLO (Carrasco et al. 2014b)

$$P_{\text{EFT}}(k, z) = P_{\text{SPT}}(k, z) + P_{c_0}(k, z), \quad (12)$$

where the tree-level counterterm is given by

$$P_{c_0}(k, z) = -2 c_0(z) [D(z)]^2 k^2 P_{\text{L}}(k), \quad (13)$$

and c_0 is undetermined by the theory. In terms of the effective speed of sound for the perturbations, $c_{s(1)}(z)$, we have $\bar{c}_0 \equiv (2\pi) [D(z)]^\zeta [c_{s(1)}(z)]^2 / k_{\text{NL}}^2$. Note that our c_0 relates to the parameter \bar{c}_1 introduced by Angulo et al. (2015) as $c_0 \equiv \bar{c}_1 [D(z)]^\zeta$ where $[D(z)]^{n+\zeta}$ is the assumed growth factor of the EFT corrections to the SPT density fluctuations of order n .

Similarly, for the bispectrum to NLO, EFT gives four counterterms (Angulo et al. 2015; Baldauf et al. 2015b)

$$B_{\text{EFT}} = B_{\text{SPT}} + B_{c_0} + B_{c_1} + B_{c_2} + B_{c_3}. \quad (14)$$

(where the dependence on $\mathbf{k}_1, \mathbf{k}_2, \mathbf{k}_3$ and z is left implicit to simplify notation), one of which is also proportional to c_0

$$B_{c_0} = c_0(z) [D(z)]^4 \left[2 P_{\text{L}}(k_1) P_{\text{L}}(k_2) \tilde{F}_2^{(s)}(\mathbf{k}_1, \mathbf{k}_2) + 2 \text{ perms.} - 2 k_1^2 P_{\text{L}}(k_1) P_{\text{L}}(k_2) F_2(\mathbf{k}_1, \mathbf{k}_2) + 5 \text{ perms.} \right], \quad (15)$$

with

$$\begin{aligned} \tilde{F}_2^{(s)}(\mathbf{k}_1, \mathbf{k}_2) = & -\frac{1}{(1+\zeta)(7+2\zeta)} \left[\left(5 + \frac{113\zeta}{14} + \frac{17\zeta^2}{7} \right) (k_1^2 + k_2^2) \right. \\ & + \left(7 + \frac{148\zeta}{7} + \frac{48\zeta^2}{7} \right) \mathbf{k}_1 \cdot \mathbf{k}_2 + \left(2 + \frac{59\zeta}{7} + \frac{18\zeta^2}{7} \right) \\ & \times \left(\frac{1}{k_1^2} + \frac{1}{k_2^2} \right) (\mathbf{k}_1 \cdot \mathbf{k}_2)^2 + \left(\frac{7}{2} + \frac{9\zeta}{2} + \zeta^2 \right) \left(\frac{k_1^2}{k_2^2} + \frac{k_2^2}{k_1^2} \right) \\ & \left. \times \mathbf{k}_1 \cdot \mathbf{k}_2 + \left(\frac{20\zeta}{7} + \frac{8\zeta^2}{7} \right) \frac{(\mathbf{k}_1 \cdot \mathbf{k}_2)^3}{k_1^2 k_2^2} \right]. \quad (16) \end{aligned}$$

Following Angulo et al. (2015), we assume $\zeta = 3.1$ as suggested by some theoretical considerations and fits to simulations (Foreman & Senatore 2016). We note that Baldauf et al. (2015c) find no appreciable difference between using $\zeta = 2$ or 3.1. Quadratic contributions from the long-wavelength perturbations to the effective-stress-tensor expansion lead to four additional counterterms, only

three of which are independent. They have the following forms:

$$B_{c_1} = -2 c_1(z) [D(z)]^4 k_1^2 P_L(k_2) P_L(k_3) + 2 \text{ perms.}, \quad (17)$$

$$B_{c_2} = -2 c_2(z) [D(z)]^4 k_1^2 \frac{(\mathbf{k}_2 \cdot \mathbf{k}_3)^2}{k_2^2 k_3^2} P_L(k_2) P_L(k_3) + 2 \text{ perms.}, \quad (18)$$

$$B_{c_3} = -c_3(z) [D(z)]^4 (\mathbf{k}_2 \cdot \mathbf{k}_3) \left[\frac{\mathbf{k}_1 \cdot \mathbf{k}_2}{k_2^2} + \frac{\mathbf{k}_1 \cdot \mathbf{k}_3}{k_3^2} \right] P_L(k_2) P_L(k_3) + 2 \text{ perms.}, \quad (19)$$

where the effective coupling constants c_1 , c_2 and c_3 are unknown (similar to c_0 , we absorb the $[D(z)]^\zeta$ scaling in their definition).

Although some authors claim that EFT provides a manifestly convergent perturbative scheme for $k < k_{\text{NL}}$ (e.g. Carrasco et al. 2014a), there are indications that, like SPT, it forms an asymptotic expansion in which adding higher and higher-loop corrections, at a certain point, deteriorates the agreement with numerical simulations (e.g. Pajer & van der Woude 2018; Konstandin et al. 2019). The break down of the theory should not be caused by the influence of short-distance physics but rather to large contributions coming from mildly non-linear scales.

At the end of the day, EFT can also be simply seen as an improved version of SPT in which counterterms are added to regularise the UV-sensitive contributions.

2.6 IR resummation

Large-scale flows broaden and damp the baryon-acoustic-oscillation (BAO) feature imprinted in P_L at early epochs. These effects are poorly captured by Eulerian perturbation theories and are more easily understood in the Lagrangian framework (Meiksin et al. 1999; Crocce & Scoccimarro 2008; Taruya et al. 2009). It turns out that it is possible to account for them by resumming the perturbative predictions to all orders, a procedure known as ‘IR resummation’ (e.g. Senatore & Zaldarriaga 2015). In the framework of EFT, this is often implemented following the strategy delineated by Baldauf et al. (2015a) and further developed in Blas et al. (2016, the method we use) and Ivanov & Sibiriyakov (2018). In order to decompose the linear power spectrum in smooth and oscillating parts, we use one-dimensional Gaussian smoothing as described in Vlah et al. (2016, appendix A) and Osato et al. (2019).

2.7 Time evolution

In all the results described above, time evolution is entirely captured by the function $D(z)$. This directly follows from equation (3) and its analogue for the EFT corrections² which hold true in the EdS universe only. In general, the second-order SPT solution has the form $D_{2A}(z) A(\mathbf{k}) + D_{2B}(z) B(\mathbf{k})$ where $D_{2A}(z)$ and $D_{2B}(z)$ slightly differ from $[D(z)]^2$ (for their explicit expressions see e.g. Appendix A in Takahashi 2008). Similarly, the third-order solution contains six different growth factors that deviate a little from $[D(z)]^3$. Previous studies have shown that assuming the $[D(z)]^n$ scaling provides rather accurate approximations to the matter power spectrum and bispectrum in the Λ CDM model (e.g. Scoccimarro et al. 1998; Bernardeau et al. 2002). For $P(k)$, the leading-order contribution is unaffected since it only depends on the linear density fluctuations.

² I.e. $\delta_{\text{EFT}}(\mathbf{k}, z) = \sum_{n=1}^{\infty} [D(z)]^{n+\zeta} \delta_{\text{EFT}}^{(n)}(\mathbf{k})$ where $\delta = \delta_{\text{SPT}} + \delta_{\text{EFT}}$.

Moreover, in the relevant range of wavenumbers, deviations from the exact solution for the one-loop corrections are well below the per-cent level at $z = 1$ (Takahashi 2008). For these reasons, we can safely set $D_{2A}(z) = D_{2B}(z) = D(z)$ in our analysis of the power spectrum. On the contrary, we use the exact F_2 kernel

$$F_{2,\Lambda\text{CDM}}(\mathbf{k}_1, \mathbf{k}_2) = \frac{5}{7} \frac{D_{2A}(z)}{D(z)^2} \frac{(\mathbf{k}_1 + \mathbf{k}_2) \cdot \mathbf{k}_1}{k_1^2} + \frac{2}{7} \frac{D_{2B}(z)}{D(z)^2} \frac{(\mathbf{k}_1 + \mathbf{k}_2)^2 \mathbf{k}_1 \cdot \mathbf{k}_2}{2k_1^2 k_2^2}, \quad (20)$$

to compute the tree-level bispectrum in SPT and EFT (but not for the loop corrections). This is necessary because adopting the EdS approximation would generate systematic shifts at the per-cent level (Steele & Baldauf 2021) which are comparable with the statistical errors of the measurements extracted from our very large suites of simulations (see section 3). We revisit this issue in section 5.3.

Since we only consider the matter density field at $z = 1$, from now on, we drop the dependence on z of all functions.

3 N-BODY SIMULATIONS

In this section, we introduce the N -body simulations and the estimators we use to test the theoretical models introduced above.

3.1 Simulation suites

We use two sets of N -body simulations, named MINERVA and Eos, run using the GADGET-2 code (Springel 2005). Our main investigation is based on the MINERVA set (first presented in Grieb et al. 2016) which consists of 300 simulations each following the evolution of 1000^3 dark-matter particles in a periodic cubic box with a side length of $1500 h^{-1}$ Mpc. In order to perform some additional tests in section 5, we complement the MINERVA suite with a subset³ of the Eos suite composed of 10 realizations each containing 1536^3 particles in a periodic cubic box with a side length of $2000 h^{-1}$ Mpc.

The simulations follow the formation of the large-scale structure in flat Λ CDM cosmological models with parameters given in Table 1. The linear transfer functions are obtained from the Boltzmann codes CAMB (Lewis et al. 2000; Howlett et al. 2012) and CLASS (Blas et al. 2011) for the MINERVA and Eos simulations respectively. In all cases, the initial particle displacements are computed using the publicly available code 2LPTIC (Crocce et al. 2006) starting from Gaussian initial conditions.

3.2 Power spectrum and bispectrum estimators

We use the POWERI4 code (Sefusatti et al. 2016) to estimate the matter density in a regular Cartesian grid containing 512^3 cells from the particle positions. With the FFT algorithm, we obtain the Fourier-space overdensity $\delta_{\mathbf{q}}$ sampled at the wavevectors \mathbf{q} with Cartesian components that are integer multiples of the fundamental frequency $k_F = 2\pi/L_{\text{box}}$. Our power-spectrum estimator is

$$\hat{P}(k) = \frac{1}{L_{\text{box}}^3 N_P} \sum_{\mathbf{q} \in k} |\delta_{\mathbf{q}}|^2, \quad (21)$$

³ Information on the Eos suite is available in Biagetti et al. (2017) and at <https://mbiagetti.gitlab.io/cosmos/nbody/eos/>.

Name	n_s	h	Ω_b	Ω_m	σ_8	# sims	$N_p^{1/3}$	L_{box} [h^{-1} Mpc]	V_{tot} [h^{-3} Gpc 3]	m_p [$10^{10} h^{-1} M_\odot$]	IC	z_{initial}
MINERVA	0.9632	0.695	0.044	0.285	0.828	300	1000	1500	1012	26.7	2LPT	63
Eos	0.967	0.7	0.045	0.3	0.85	10	1536	2000	80	18.3	2LPT	99

Table 1. Cosmological and structural parameters for the MINERVA and Eos simulations.

s	c	N_k	N_t	k_{max} [h Mpc $^{-1}$]
1	2.0	48	11757	0.20
2	2.5	28	2513	0.24
3	3.0	28	2513	0.36

Table 2. Main characteristics of our binning schemes –see equation (23). The total number of measurements for \hat{P} and \hat{B} are indicated with N_k and N_t , respectively, while k_{max} gives the maximum wavenumber reached.

where N_P is the number of \mathbf{q} vectors lying in a bin centred at wavenumber k and of width Δk . The notation $\mathbf{q} \in k$ means that $k - \Delta k/2 \leq q < k + \Delta k/2$. Similarly, for the bispectrum, we use

$$\hat{B}(k_1, k_2, k_3) = \frac{1}{L_{\text{box}}^3 N_B} \sum_{\mathbf{q}_1 \in k_1} \sum_{\mathbf{q}_2 \in k_2} \sum_{\mathbf{q}_3 \in k_3} \delta_{\mathbf{q}_1} \delta_{\mathbf{q}_2} \delta_{\mathbf{q}_3}, \quad (22)$$

where \mathbf{q}_1 , \mathbf{q}_2 and \mathbf{q}_3 satisfy the triangle condition $\mathbf{q}_{123} = 0$ and N_B denotes the number of triangles contributing to a given ‘triangle bin’ defined by the sides $k_1 \geq k_2 \geq k_3$ (which do not necessarily form a closed triangle, Oddo et al. 2020). We consider different binning schemes characterised by the bin width $s = \Delta k/k_F$ and the central wavenumber of the first bin c (also expressed in units of k_F) so that the centres of all bins are given by

$$k_i = [c + (i - 1)s] k_F, \quad i = 1, 2, \dots, N_k. \quad (23)$$

The parameters we use for the different power-spectrum and bispectrum measurements and the maximum wavenumber they reach are summarised in Table 2. It is worth stressing that we subtract from \hat{P} and \hat{B} the systematic contributions due to Poissonian shot noise which are anyway smaller than the statistical uncertainties.

Fig. 1 shows the average \hat{P} obtained from the MINERVA simulations for the three bin sizes (top panel) and the relative standard error of the mean (bottom panel). Note that, due to the large number of realisations we consider, we achieve better than one-per-cent (one-per-mille) precision for $k > 0.01 h \text{ Mpc}^{-1}$ ($k > 0.1 h \text{ Mpc}^{-1}$). Similarly, Fig. 2 shows the mean \hat{B} (top panels) and its standard deviation (bottom panels). In this case, the relative errors range between 10 per cent and one per mille depending on the triangular configuration and the bin size. Dealing with such unusually small random errors (which cannot be obtained from current observations of galaxy clustering) calls for a consistent treatment of the systematic errors introduced by the N -body method (see section 5.4).

4 MATCHING THE MODELS TO SIMULATIONS

In this section, we explain how we compare the perturbative models to the measurements extracted from the N -body simulations.

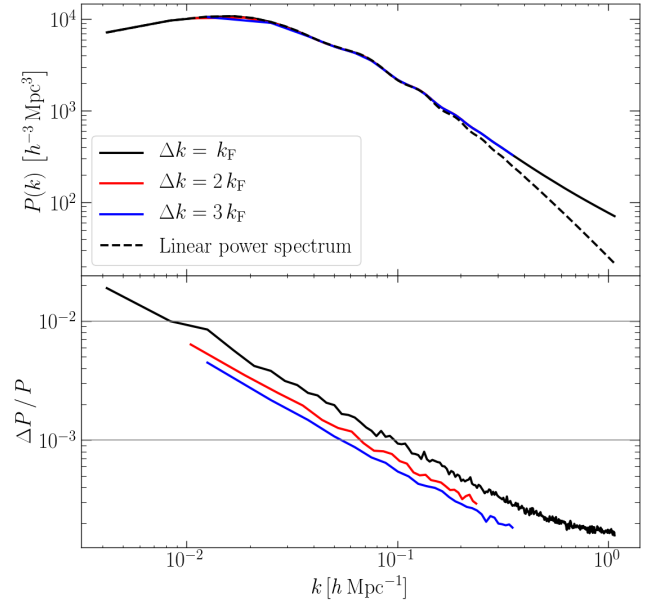


Figure 1. The mean power spectrum extracted from the MINERVA simulations (top) and the corresponding statistical uncertainty (bottom).

4.1 Binning of theoretical predictions

In order to compare the theoretical predictions with the measurements, we need to account for the finite bin sizes assumed by the power-spectrum and bispectrum estimators and, possibly, for the discreteness characterising the Fourier-space density grid. The most precise approach to the problem⁴ consists of averaging the theoretical predictions over the same set of configurations as it is done for the estimators (21) and (22). Taking these averages, however, is computationally demanding, at least for the bispectrum. A considerable speedup (at the expense of accuracy) can be achieved by computing the model predictions for one characteristic configuration per triangle bin. For instance, Sefusatti et al. (2010) considered the average value of the triplet (k_1, k_2, k_3) in a bin that from now on we refer to as the ‘effective’ triangle of a bin. In what follows, we always use the full average of the theoretical predictions for the power spectrum and the tree-level bispectrum. On the other hand, due to the computational demand, we average the loop corrections for B only for triangle bins with $k_3 \lesssim 0.14 h \text{ Mpc}^{-1}$. In all the other cases, we evaluate the corrections using one effective triangle per bin (after checking that this approximation is accurate enough on the larger scales for which we have the average).

⁴ With the exception of point-by-point comparisons on individual realisations (Roth & Porciani 2011; Taruya et al. 2012, 2018; Steele & Baldauf 2021).

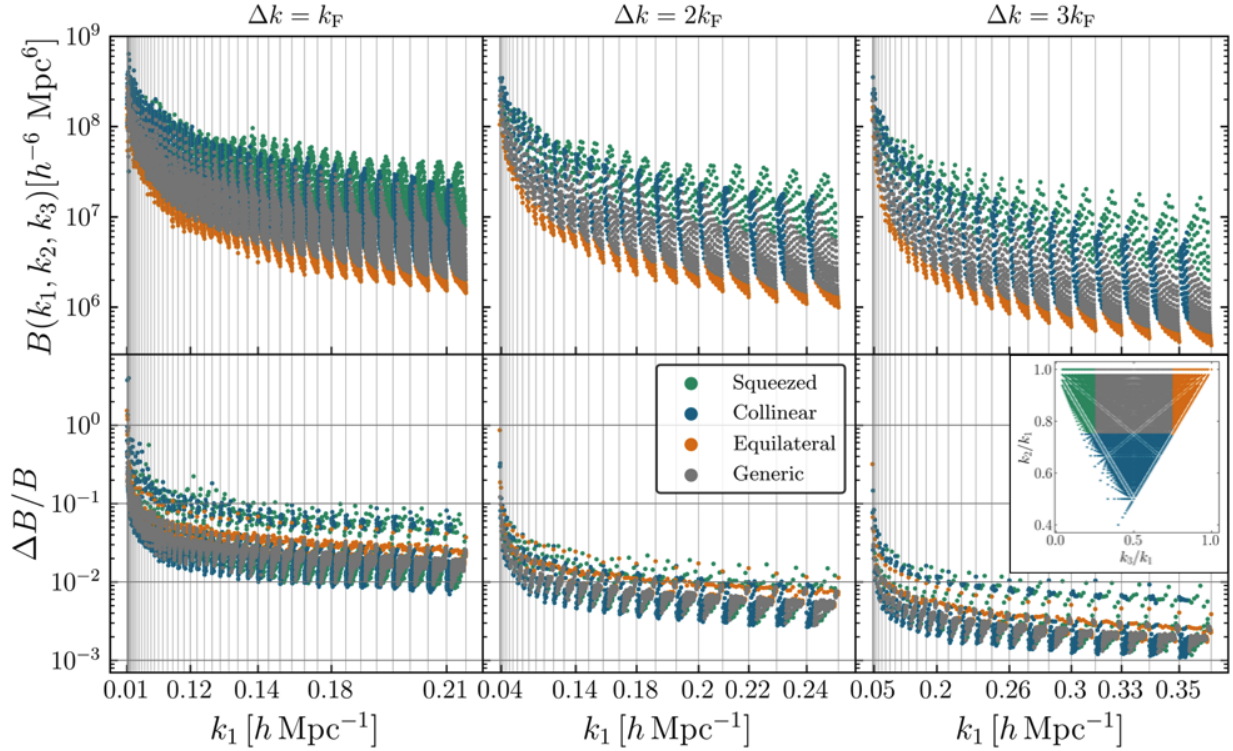


Figure 2. The mean bispectrum extracted from the MINERVA simulations (top) and its statistical uncertainty (bottom). Results are plotted by ordering the triangular configurations as in [Oddo et al. \(2020\)](#). In between two consecutive vertical lines, all points correspond to triangle bins with the same longest side k_1 , whereas k_2 and k_3 take all allowed values. The color of the symbols indicates different triangular shapes as illustrated in the bottom middle and right panels.

4.2 Goodness of fit

In order to quantify the goodness-of-fit of the different models, we assume Gaussian errors and rely on the χ^2 test. Schematically, given the mean measurements from the simulations, $\langle D_i \rangle$, and the corresponding model predictions, M_i , we compute the statistic

$$\chi_m^2 = \frac{\chi_{\text{tot}}^2}{\nu} = \frac{1}{\nu} \sum_{i,j} (M_i - \langle D_i \rangle) C_{ij}^{-1} (M_j - \langle D_j \rangle), \quad (24)$$

where ν indicates the number of degrees of freedom (i.e. the number of data points N minus the number of adjusted parameters), the indices i and j run over all possible configurations, and C_{ij} denotes the elements of the covariance matrix for the adopted estimators (or some approximation thereof).

Since we only consider relatively large scales, we use the so-called Gaussian contribution to the covariance matrix for the power-spectrum estimates, ([Feldman et al. 1994](#); [Meiksin & White 1999](#))

$$C_{ij} = \frac{2 P_i^2}{N_P} \delta_{ij}, \quad (25)$$

with P_i the expected power spectrum in the i^{th} bin and δ_{ij} the Kronecker symbol. In order to prevent that the covariance is informed about the noise in our realisations, we use a smooth function to compute P_i in the expression above. This is obtained by fitting the outcome of the MINERVA simulations with the expression ([Cole et al. 2005](#))

$$P_{\text{NL}}(k) = P_{\text{L}}(k) \left(\frac{1 + Qk^2}{1 + Ak} \right), \quad (26)$$

where Q and A are free parameters. We find that setting $Q \approx 4 h^{-2} \text{Mpc}^2$ and $A \approx 0.37 h^{-1} \text{Mpc}$ provides a fit that agrees with the measurements to better than one per cent at all the scales considered in this work.

For the bispectrum, we find that, even at large scales, the Gaussian approximation underestimates the sample variance from numerical simulations in a shape-dependent manner, reaching a difference of order 50 per cent for some squeezed-triangle configurations (see also [Chan & Blot 2017](#); [Colavincenzo et al. 2019](#); [Gualdi & Verde 2020](#)). For this reason, we use the approximate expression

$$C_{ij} = [(PPP)_i + 2(BB)_i] \delta_{ij}, \quad (27)$$

where

$$(PPP)_i \approx \frac{6 L_{\text{box}}^3}{N_B} \overline{P_{\text{NL}}(k_1) P_{\text{NL}}(k_2) P_{\text{NL}}(k_3)} \quad (28)$$

denotes the Gaussian part and the overline indicates the average over all the configurations contributing to the i^{th} triangle bin while

$$(BB)_i \approx (B_{\text{NL}}^{\text{eff}})^2 \left[\frac{1}{N_P(k_1)} + \frac{1}{N_P(k_2)} + \frac{1}{N_P(k_3)} \right], \quad (29)$$

where $B_{\text{NL}}^{\text{eff}}$ denotes the tree-level bispectrum in SPT evaluated at the effective wavenumbers using P_{NL} instead of P_{L} . The $(BB)_i$ term approximates the actual non-Gaussian contribution due to configurations that share one k -bin (see, e.g. [Sefusatti et al. 2006](#)). Note that the factor of two in equation (27) is meant to approximately compensate for the additional contribution to the covariance that scales as the product of the power spectrum and the trispectrum.

In order to assess the accuracy of these approximations to the

covariance matrices for \hat{P} and \hat{B} , we use the statistic

$$\chi_s^2 = \frac{1}{N} \text{Tr}(\mathbf{S}\mathbf{C}^{-1}), \quad (30)$$

where \mathbf{S} denotes the sample covariance matrix of the measurements from the MINERVA simulations and \mathbf{C} is our model covariance. It is possible to show that, for Gaussian errors with covariance matrix \mathbf{C} , the statistic $N\chi_s^2$ follows a chi-square distribution with N degrees of freedom (Porciani 2021). Therefore, our approximations for the covariance matrix should be considered inaccurate if χ_s^2 strongly departs from unity. In this case, any conclusion on the accuracy of the models based on χ_m^2 should be disregarded. Note that our approximations for the covariance matrices are diagonal, implying that

$$\chi_s^2 = \frac{1}{N} \sum_{i=1}^N \frac{S_{ii}}{C_{ii}}. \quad (31)$$

i.e. χ_s^2 gives the average ratio between the measured and assumed variances of the different data points.

Before moving on, it is important to note that we do not account for the so-called ‘theoretical errors’ – i.e. uncertainties on the perturbative predictions reflecting the estimated size of the higher-order terms that are neglected – as advocated by some authors (e.g. Baldauf et al. 2016; Steele & Baldauf 2021; Chudaykin et al. 2021). The reason is very simple. We are not trying to determine the domain of validity of the full perturbative expansion (we are actually agnostic regarding its convergence). More pragmatically, we simply want to find out the range of scales for which the one-loop formulae provide an accurate match to N -body simulations.

In the remainder of this paper, we distinguish between the concepts of accuracy and validity: the former indicates how closely a perturbative expansion reproduces the exact answer while the latter refers to the consistency of all the assumptions of the theory. Therefore, the domain of accuracy and the range of validity of the models should not be confused. For instance, a model could still provide a good approximation to the truth on a range of scales although its assumptions are not valid.

5 RESULTS

In this section, we determine the domain of accuracy of the perturbative models for the matter power spectrum and bispectrum we have introduced in section 2 by comparing them against N -body simulations. To start with, we pay particular attention to discussing how we fix the EFT parameters that determine the amplitude of the counterterms. Subsequently, we present results as a function of the total volume used to measure P and B . As a final step, we discuss the impact of systematic errors introduced by the N -body technique.

5.1 EFT parameters

As mentioned in section 2.5, the EFT parameters related to the counterterms need to be determined from the simulation data. In doing so, we do not distinguish between the actual counterterms and the renormalised contributions. Therefore, the coefficients we obtain should be interpreted as simple ‘matching coefficients’ and not given any particular physical interpretation. Following a common trend in the literature, we will keep referring to these coefficients as counterterms.

The EFT power spectrum at one loop only contains the parameter c_0 for which, following Baldauf et al. (2015b), we can build an estimator starting from equations (12) and (13),

$$\hat{c}_0(k) = -\frac{\langle \hat{P}(k) \rangle - P_{\text{SPT}}(k)}{2k^2 P_L(k)}. \quad (32)$$

In the left panel of Fig. 3, we show how \hat{c}_0 depends on k when we use the mean power spectrum extracted from the MINERVA simulations. Within the EFT framework, c_0 is a scale-independent parameter but our data show that \hat{c}_0 significantly deviates from its low- k limit when $k > 0.14 h \text{ Mpc}^{-1}$. This is usually interpreted as a signal that the truncated perturbative expansion breaks down beyond this scale and higher-order corrections become important (Foreman et al. 2016). In the right panel of Fig. 3, we determine c_0 by fitting P_{EFT} (with and without IR resummation) to the mean power spectrum extracted from the MINERVA simulations. Our results are shown as a function of the maximum wavenumber used in the fit, k_{fit} . The orange line represents the best-fitting value for the EFT model and the shaded region around it marks the 68-per-cent confidence region of the fit. Not surprisingly, it resembles a smoothed version of the results shown in the left panel. Considering subsets of 23 MINERVA boxes (which cover the same total volume as the Eos simulations) only increases the scatter of the estimates (blue shaded region). Accounting for the IR resummation (green line) removes the oscillations in the region of the baryonic acoustic features but does not attenuate the overall scale dependence for $k > 0.14 h \text{ Mpc}^{-1}$. Based on these results, we conclude that the domain of validity of the one-loop EFT expressions for the power spectrum at $z = 1$ is $k < 0.14 h \text{ Mpc}^{-1}$. Our results are consistent with fig. 14 of Baldauf et al. (2015b), even though our analysis is performed at $z = 1$ instead of $z = 0$. Remarkably, the limiting value we find is also consistent with the blinded challenge presented in Nishimichi et al. (2020), which uses a total simulation volume of $566 h^{-3} \text{ Gpc}^3$ (about half of the volume covered by the MINERVA suite) at $z = 0.61$ to test the constraining power for cosmology of the EFT predictions for the galaxy power spectrum in redshift space. In this case, the recovered cosmological parameters show a bias whenever the mock data sets are extended beyond $k_{\text{max}} = 0.14 h \text{ Mpc}^{-1}$. In the remainder of this paper, we use the best-fitting value of c_0 using $k_{\text{fit}} = 0.14 h \text{ Mpc}^{-1}$ as the default option for P_{EFT} . This gives $c_0 = 0.581 \pm 0.009 h^{-2} \text{ Mpc}^2$. If we simply rescale this value by $[D(z = 1)]^{-2}$ (thus ignoring any intrinsic time dependence of c_0), we obtain 1.525 which closely matches the results previously obtained at $z = 0$ using slightly different cosmological models, methods, and scales (Carrasco et al. 2014b; Angulo et al. 2015; Baldauf et al. 2015c).

The EFT bispectrum at one loop contains four unknown parameters and different strategies have been developed in the literature to determine them. For instance, it is possible to express c_1, c_2 and c_3 as a function of c_0 by imposing renormalisation conditions and then fix c_0 from a fit to the power spectrum (Angulo et al. 2015; Baldauf et al. 2015c). An alternative line of attack – which we follow here – is to treat (at least some of) the EFT parameters as fit parameters for the bispectrum, trying to avoid overfitting. The recent and comprehensive study by Steele & Baldauf (2021) gives evidence supporting the second approach. Two options are available when fitting c_0 : we can either use the value that best fits the power spectrum or determine it together with the other EFT parameters only using the bispectrum. We compare these alternatives in Fig. 4, where we show the dependence of the best-fitting EFT parameters on the maximum wavenumber considered in the fit. In all cases, we use the IR resummed model. Focussing on c_0 , we notice that the fit based on the power spectrum is much more

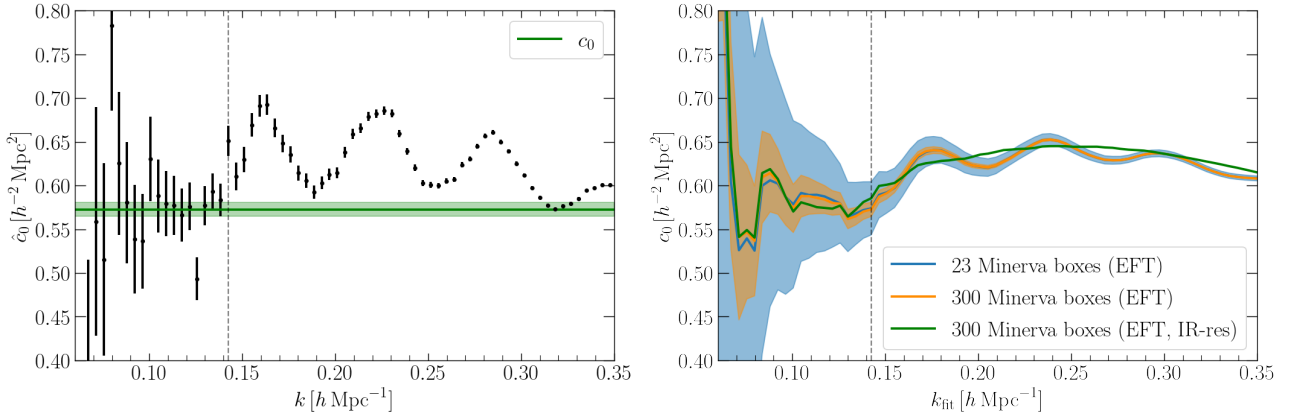


Figure 3. The EFT parameter c_0 obtained by matching the model for the power spectrum at one loop to the MINERVA simulations. In the left panel, we use the estimator given in equation (32), while, in the right panel, we fit the model to the numerical data for $k < k_{\text{fit}}$. Shown are the best-fitting values (solid lines) and their uncertainty (68-per-cent confidence interval, shaded regions). As indicated in the legend, different colours distinguish results obtained with and without accounting for IR resummation or by considering subsamples of the MINERVA simulations. To improve readability, we do not plot the shaded region for the IR-resummed EFT case. The vertical line indicates the scale at which a statistically significant departure from the low- k limit is detected for the full data set. The horizontal line in the left panel shows the result of the fit in the right panel for $k_{\text{fit}} = 0.14 \text{ h Mpc}^{-1}$.

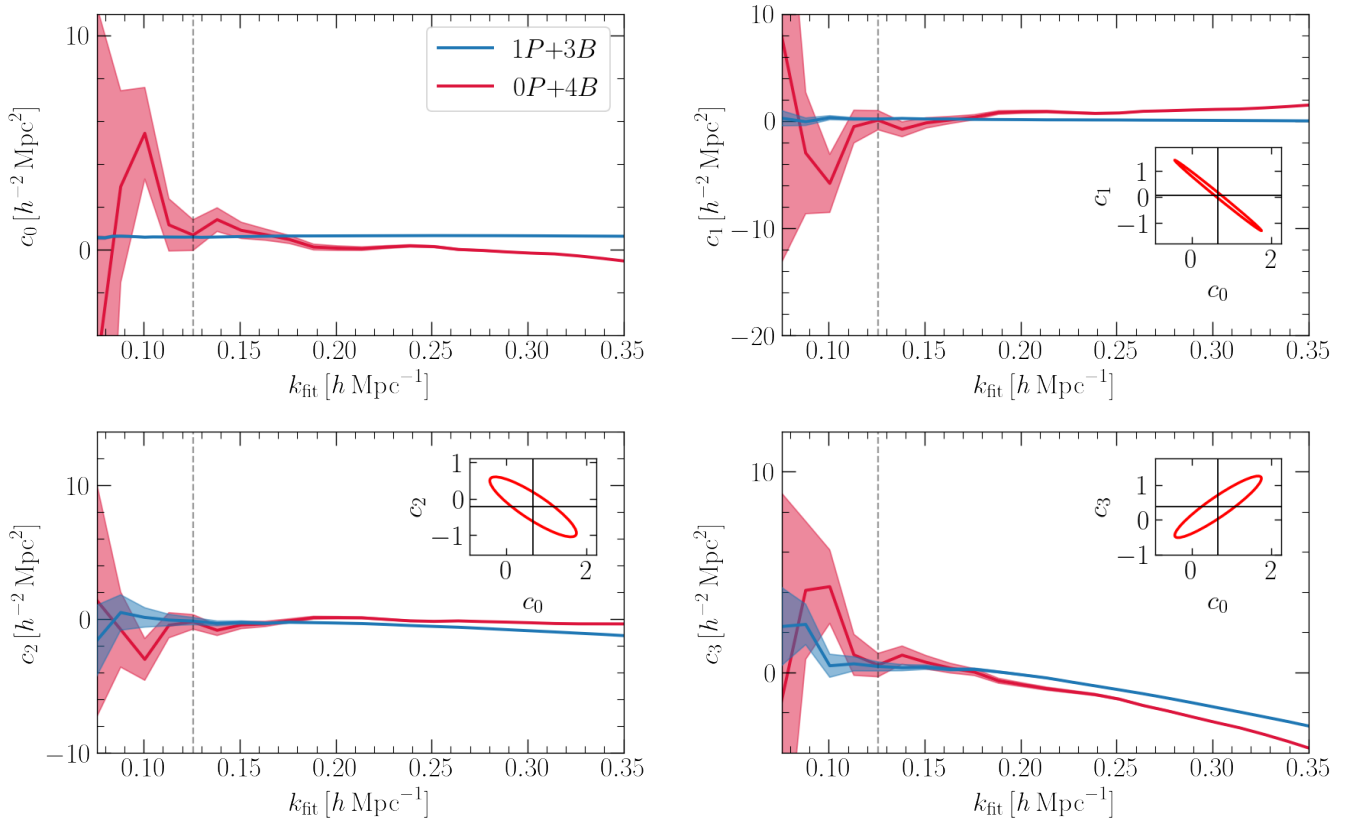


Figure 4. The best-fitting values (solid lines) and the uncertainties (shaded regions) of the EFT parameters that influence the matter bispectrum at one loop are shown as a function of the maximum wavenumber of the measurements extracted from the MINERVA simulations. We consider two cases: (i) we fix c_0 using the power spectrum (Fig. 3) and the other three parameters using the bispectrum (blue) and (ii) we fit all four parameters using the bispectrum measurements (red). The vertical dashed lines indicate the default value of $k_{\text{fit}} = 0.125 \text{ h Mpc}^{-1}$ we use in the remainder of the paper. The insets show the joint 68-per-cent confidence regions for two EFT parameters evaluated for $k_{\text{fit}} = 0.125 \text{ h Mpc}^{-1}$. The cross indicates the best-fitting values of these parameters.

stable and less uncertain at large scales. It is also worth stressing that the best-fitting values are sometimes negative while $c_0 \geq 0$ in the theory. However, we do not give much weight to this consideration since we do not fit the renormalised counterterms. We also notice that c_0 and the other EFT parameters are strongly correlated when they are simultaneously fit from the bispectrum. Their trend with k_{fit} in Fig. 4 clearly shows that this happens at all scales. Such degeneracy is investigated in more detail in the three insets where we show the joint 68.3-per-cent confidence region for c_0 and a second parameter estimated at $k_{\text{fit}} = 0.125 \text{ h Mpc}^{-1}$ while keeping the remaining two fixed at their best-fitting values. The cross-correlation coefficients between c_0 and the other parameters are as high as -0.997 (c_1), -0.872 (c_2) and 0.922 (c_3) indicating that the bispectrum data cannot isolate the contributions from the different counterterms. We believe that the large-scale fluctuations of the EFT parameters are largely influenced by this degeneracy. The fluctuations are, in fact, greatly suppressed by fixing c_0 to the best-fitting value from the power spectrum. In this case, the four EFT parameters assume consistent values for $k_{\text{fit}} < 0.14 \text{ h Mpc}^{-1}$ (which is basically determined by P). On the contrary, considering smaller scales generates deviations, especially for c_0 and c_3 . All this suggests that $k = 0.14 \text{ h Mpc}^{-1}$ also approximately delimits the domain of validity of the one-loop model for the bispectrum at $z = 1$. However, the two fitting methods (i.e. fitting three or four counterterms with the bispectrum) do not provide fully consistent results for all parameters at $k_{\text{fit}} \approx 0.14 \text{ h Mpc}^{-1}$ while they do at $k_{\text{fit}} \approx 0.125 \text{ h Mpc}^{-1}$ (the actual values are listed in Table 3). For this reason, unless explicitly stated otherwise, from now on we fix the EFT parameters for B_{EFT} to the best-fitting values at this scale using the power spectrum to determine c_0 and the bispectrum to measure c_1, c_2 and c_3 . Note that, in spite of our unprecedentedly large data set, only c_0 is precisely determined while c_1, c_2 and c_3 are compatible with being zero within a few standard deviations. This suggests that it might be quite challenging to fix the EFT counterterms for the bispectrum from actual observational data and all what could be done is to marginalise over them in a Bayesian fashion, possibly reducing the constraining power for cosmology of the data.

5.2 Power spectrum

If we assume for the moment that the N -body technique does not introduce any systematic shifts, we can determine the domain of accuracy of the perturbative models for the matter power spectrum by directly comparing their predictions to the measurements extracted from the numerical simulations. The huge volume covered by the MINERVA simulations results in sub-per-cent statistical uncertainties for the average power spectrum (see Fig. 1). Getting agreement to this precision would be a major achievement for the models.

In the top panel of Fig. 5, we show the mean power spectrum extracted from the MINERVA simulations using $\Delta k = k_{\text{F}}$ (symbols with error bars) and the corresponding bin-averaged models (solid lines with different colours as indicated by the label). In order to reduce the span of the data and improve readability, we plot the deviation from the linear power spectrum in per-cent points. Similarly, in the second panel from the top, we show the same measurements and models but in terms of their deviation with respect to P_{EFT} which provides a better fit to the numerical data. The third panel, instead, shows the χ_m^2 statistic evaluated for the different models as a function of k_{max} . This quantity gives a measure of the goodness of fit. In order to have a reference scale, we highlight the regions bounded by the one-sided upper and lower 95 per cent confidence

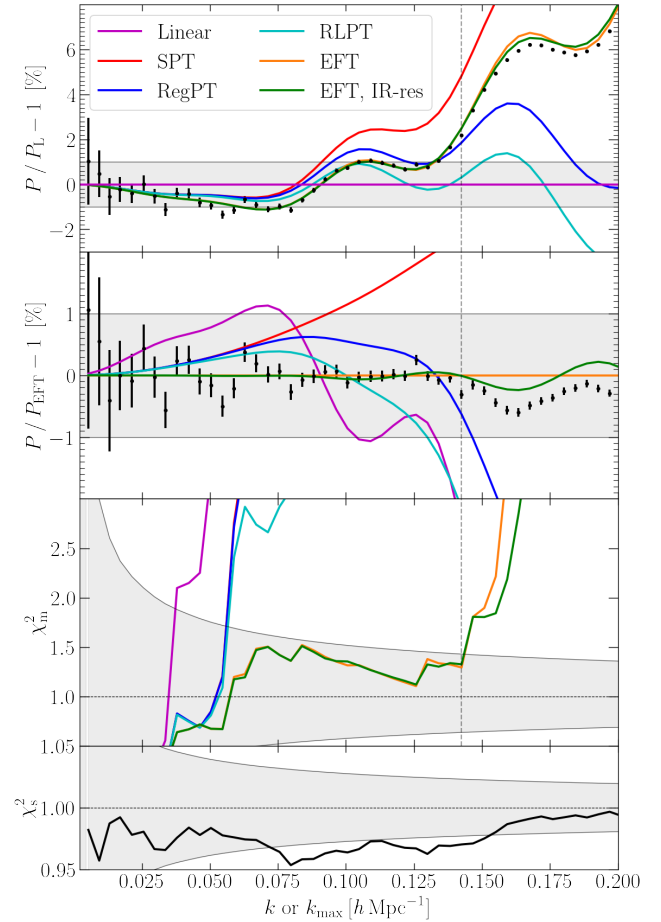


Figure 5. Comparison of the perturbative models for the matter power spectrum (solid lines) with the mean measurement extracted from the MINERVA simulations (symbols with error bars) using the bin width $\Delta k = k_{\text{F}}$. The top two panels compare the different power spectra to P_{L} and P_{EFT} whereas the bottom two display the goodness of fit for the models and the covariance matrix (see section 4.2 for details). The grey shaded areas in the top two panels represent deviations smaller than one per cent with respect to the reference models. Those in the bottom two panels, instead, mark the regions bounded by the upper and lower 95 per cent confidence limits for the χ^2 distribution with the appropriate number of degrees of freedom. The vertical dotted line indicates $k_{\text{fit}} = 0.14 \text{ h Mpc}^{-1}$ which is the largest wavenumber used to fit c_0 for the EFT models.

limits for the χ^2 statistic (with the appropriate number of degrees of freedom) with a grey shaded region. Basically, a model should be rejected at 95 per cent confidence when its χ_m^2 lies outside the shaded region. In practice, we determine the domain of accuracy of the models as follows: moving from left to right, we look for the first k_{max} at which χ_m^2 lies outside the shaded region. Finally, the bottom panel shows the χ_s^2 statistic as a function of k_{max} together with the corresponding 95 per cent confidence limits that can be used to evaluate the quality of our approximation for the covariance matrix.

Coming to the specific outcome of this comparison, Fig. 5 indicates that, although equation (25) systematically overestimates the variance of our measurements by a few percent, this discrepancy is hardly statistically significant in the range of scales we consider. Moreover, by examining the χ_m^2 curves as a function of k_{max} , it is evident that, when a model begins to break down, χ_m^2 increases very steeply so that the inferred reach is quite insensitive

Fit	χ_m^2	c_0 [$h^{-2} \text{Mpc}^2$]	c_1 [$h^{-2} \text{Mpc}^2$]	c_2 [$h^{-2} \text{Mpc}^2$]	c_3 [$h^{-2} \text{Mpc}^2$]
$1P + 3B$	171.03/167	0.577 ± 0.013	0.177 ± 0.071	-0.16 ± 0.27	0.30 ± 0.23
$0P + 4B$	171.01/166	0.67 ± 0.72	0.06 ± 0.90	-0.22 ± 0.54	0.37 ± 0.58

Table 3. Best-fitting values and uncertainties of the EFT parameters derived with $k_{\text{fit}} = 0.125 h \text{Mpc}^{-1}$ in Fig. 4. The χ_m^2 statistic for the best fit is expressed in terms of χ_{tot}^2 and ν as in equation (24).

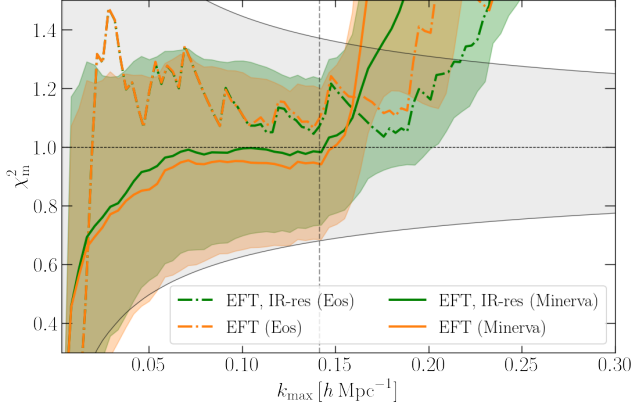


Figure 6. The χ_m^2 statistic for the EFT and IR-resummed EFT power spectra evaluated using the Eos suite (dash-dotted) and many different subsets of 23 MINERVA simulations (solid and shaded for mean and standard deviation, respectively). The grey shaded area highlights the region bounded by the (one-sided) upper and lower 95-per-cent confidence limits for a χ^2 distribution function with the appropriate number of degrees of freedom. The vertical dotted line indicates k_{fit} .

to small deviations in the size of the error bars. Therefore, we can proceed further with analysing the χ_m^2 curves knowing that this statistic will be only very slightly underestimated. This provides a clear ranking for the models based on their domain of accuracy. Not surprisingly, the first model to break down is P_L which fits the MINERVA simulations only for $k_{\text{max}} < 0.035 h \text{Mpc}^{-1}$, followed by SPT ($k_{\text{max}} < 0.06 h \text{Mpc}^{-1}$). Since on these relatively large scales RegPT and RLPT essentially coincide with SPT, they also fail at the same k_{max} . Contrary to SPT, however, they agree with the simulations to better than one per cent up to $k \approx 0.15 h \text{Mpc}^{-1}$. The best agreement is found with the EFT model which fits the MINERVA simulations accurately for $k_{\text{max}} < 0.14 h \text{Mpc}^{-1}$ (and never shows per cent deviations within the explored range of wavenumbers). Consistently with previous work (e.g. Baldauf et al. 2015a), we find that IR-resummation improves the fit only beyond its nominal range of accuracy. One issue worth investigating is that the value of χ_m^2 rises sharply around $k \approx 0.125 h \text{Mpc}^{-1}$ and $0.14 h \text{Mpc}^{-1}$, which causes the EFT models to get rejected on slightly larger scales than perhaps expected (based on visual inspection of the top panel in Fig. 5). This is caused by the statistically significant deviation of two simulation data points around those scales which are clearly distinguishable in the second panel (from the top) of Fig. 5. After carefully inspecting individual simulations to understand the origin of these deviations, we could not reach any clear conclusion. However, upon re-measuring the power spectrum using narrower bins in that region, we notice that the deviations form coherent features within a range of k -values and are not simply due to random noise.

To cross check our results and also test the models under less demanding standards, we repeat our analysis using the Eos sim-

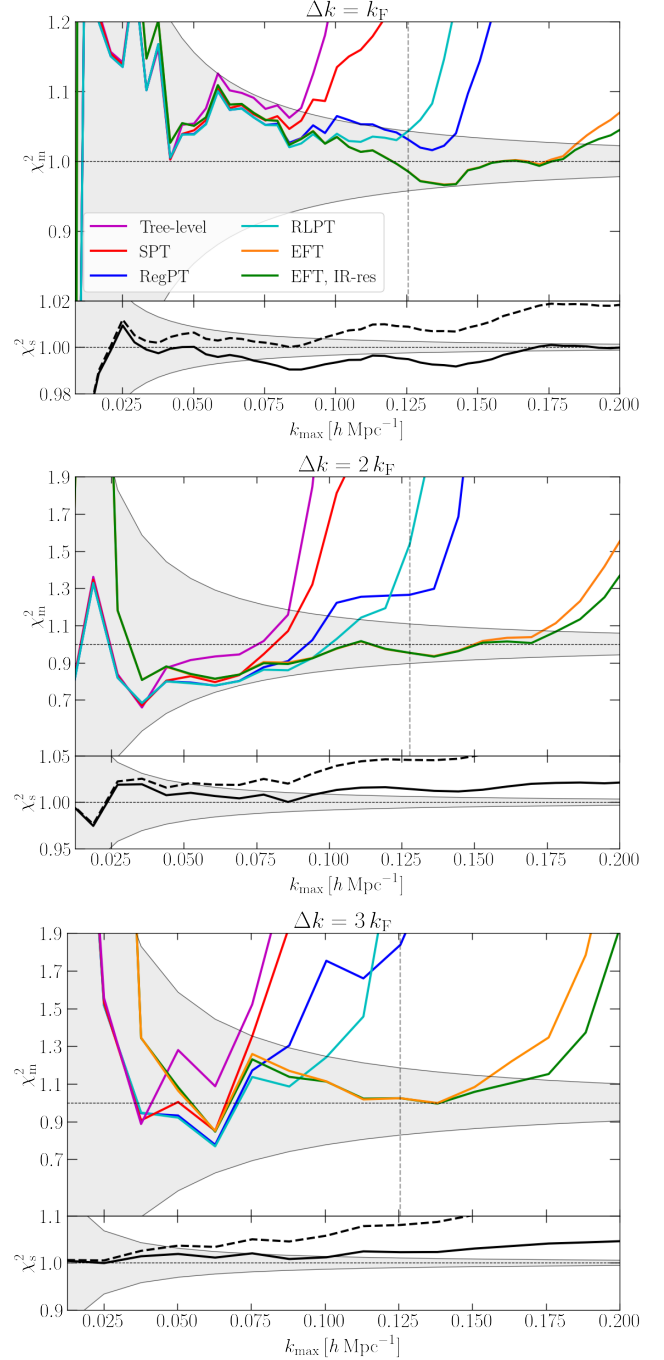


Figure 7. As in the bottom two panels of Fig. 5 but for the matter bispectrum. From top to bottom, we consider three different bin widths, namely k_F , $2 k_F$ and $3 k_F$. The dashed lines in the plots for χ_s^2 (bottom panels) refer to the Gaussian approximation to the covariance matrix.

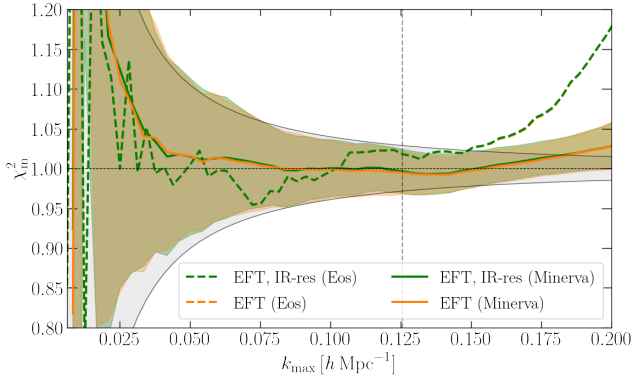


Figure 8. As in Fig. 6 but for the matter bispectrum.

ulations which cover a smaller volume (roughly corresponding to 23 MINERVA boxes) and thus give larger statistical error bars. For simplicity, we only consider the EFT models with and without IR-resummation. In order to properly compare results obtained using the MINERVA and Eos suites, we proceed as follow: (i) we random sample 23 MINERVA boxes from the full set; (ii) we fit the EFT parameter c_0 to the mean power spectrum of the subset using $k_{\max} = 0.14 h \text{ Mpc}^{-1}$; (iii) we compute the χ_m^2 statistic as a function of k_{\max} for the best-fitting c_0 . Our results are shown in Fig. 6 where the solid lines represent the mean χ_m^2 obtained from the MINERVA subsets and the shaded regions around them show the corresponding standard deviation. Overall, these findings are in very good agreement with the χ_m^2 curves derived from the Eos simulations (dot-dashed lines). Due to the larger statistical error bars, the nominal reach of the EFT models slightly increases with respect to the analysis performed with the full MINERVA set. We find $k_{\max} < 0.16^{+0.05}_{-0.01} h \text{ Mpc}^{-1}$ for standard EFT and $k_{\max} < 0.17^{+0.06}_{-0.02} h \text{ Mpc}^{-1}$ for IR-resummed EFT. Note that this extends beyond the minimum scale for which c_0 can be assumed to be constant.

5.3 Bispectrum

In Fig. 7, we investigate the goodness of fit of the different models for the matter bispectrum by plotting the χ_m^2 and χ_s^2 statistics as a function of k_{\max} for various bin sizes. In the bottom panels, we show two curves: the solid one considers our approximation to the covariance matrix given in equation (27) while the dashed one refers to the Gaussian part given in equation (28). It is evident that the Gaussian approximation severely underestimates the variance of the bispectrum measurements already at large scales and especially for broader triangle bins. On the contrary, equation (27) provides average deviations of only a few per cent for all configurations considered in this work. We believe that this is accurate enough to get robust estimates of χ_m^2 , although, at small scales, the assumed covariance matrix is nominally incompatible with the scatter seen in the simulations (i.e. the black curve lies outside the shaded region in the plots for χ_s^2).

The variations of χ_m^2 with k_{\max} provide a clear ranking of the models. Independently of the bin width, the tree-level SPT prediction breaks down first and one-loop corrections only slightly improve the range of accuracy of the theory up to $k_{\max} \approx 0.08 h \text{ Mpc}^{-1}$. RegPT and RLPT provide substantial improvements and accurately match the MINERVA simulations up to scales between $0.1 h \text{ Mpc}^{-1}$ and $0.14 h \text{ Mpc}^{-1}$ depending on the bin width. Finally,

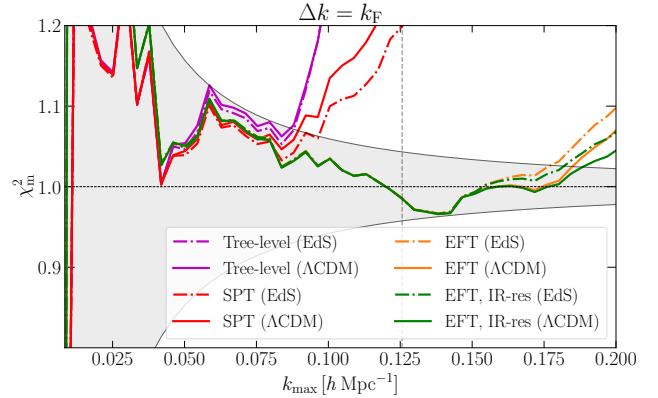


Figure 9. As in the top panel of Fig. 7 but comparing models obtained with the exact second-order SPT kernels (ACDM) and the popular EdS approximation (see the main text for details).

the counterterms in the EFT bispectra boost the agreement up to $k_{\max} \approx 0.16 - 0.19 h \text{ Mpc}^{-1}$. IR-resummation turns out to be relevant only for $k \gtrsim 0.15 h \text{ Mpc}^{-1}$ and even marginally for the case of narrow bins, where statistical errors are larger than the deviations between the model and the data at the scales of the baryonic acoustic oscillations.

As we already did with the power spectrum, in Fig. 8, we verify that using the MINERVA and Eos simulations gives consistent results for the bispectrum as well. It turns out that the reach of the EFT models is a bit reduced for the Eos simulations but this is consistent with random fluctuations. We also note that, for Eos, the EFT models with and without IR-resummation have practically the same domain of accuracy as a consequence of the larger uncertainty of the measurements.

Finally, we test the impact of using the popular EdS approximation for the second-order kernel F_2 instead of the more general scheme we described in section 2.7. Fig. 9 shows that this modification has very little influence on our results. No changes in the χ_m^2 are visible on large scales where error bars are bigger. The only noticeable differences are: (i) a slight improvement in the reach of SPT when the EdS approximation is adopted and (ii) a similarly sized increase in the range of accuracy of EFT when the exact second-order kernel is used.

5.4 Range of accuracy vs surveyed volume

The careful reader might have noticed that our results are more conservative than other estimates in the literature. This is partially due to the fact that we use all bispectrum configurations, but mostly because we use a much larger set of N -body simulations (cf. Angulo et al. 2015). Current surveys of the large-scale structure of the Universe cover volumes which are one to two orders of magnitude smaller than the total volume of the MINERVA simulations. This directly translates into larger statistical uncertainties for summary statistics like the power spectrum and the bispectrum and thus into more extended ranges of accuracy for the models. In this section, we investigate how the reach of the models depends on the volume covered by a survey. In doing so, we also need to account for systematic effects which we have so far neglected. In order to better evaluate their impact on our conclusions, we start with assuming that they are of no consequence (we relax this assumption in the next section).

In the top panels of Figs. 10 and 11, we show how the reach

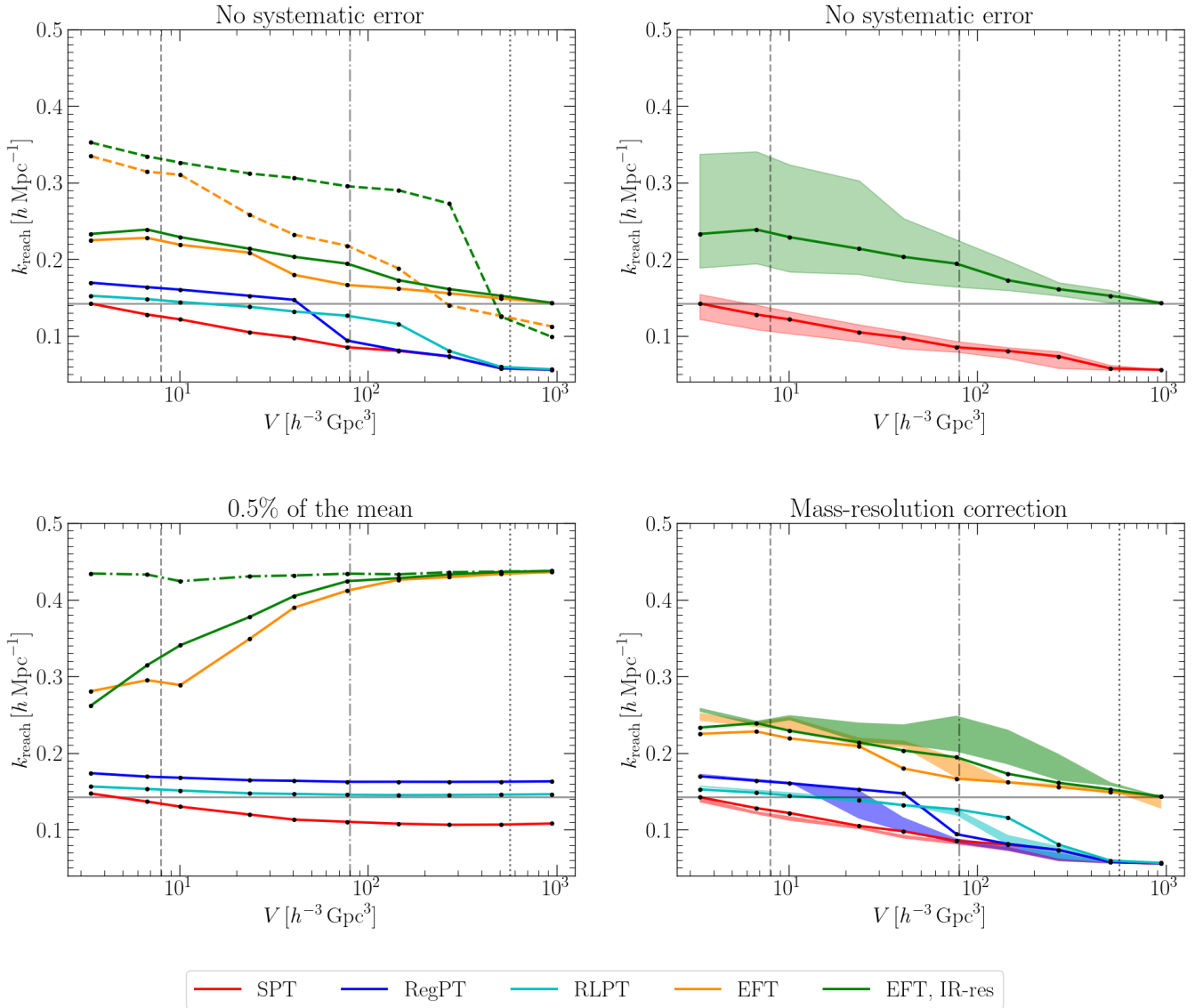


Figure 10. We define the reach of a model for the power spectrum as the minimum k_{\max} at which the χ^2 goodness-of-fit test rejects the null hypothesis that the N -body data are consistent with the model predictions at the significance level of 0.05. The top-left panel shows the median reach of 200 subsets of MINERVA simulations each covering a volume V . Different colours refer to different models as indicated in the label. Solid lines are used for the models with no free parameters and for our default EFT models (i.e. with $k_{\text{fit}} = 0.14 h \text{ Mpc}^{-1}$, highlighted by a horizontal grey line) while the two dashed lines represent the EFT models with $k_{\text{fit}} = 0.22 h \text{ Mpc}^{-1}$. The top-right panel shows the median (solid) and the central 68-per-cent range (shaded) of the estimated reach for SPT and the default IR-resummed EFT. The bottom-left panel is analogous to the top-left one but accounts for systematic errors in the simulations by considering an additional 0.5-per-cent error added in quadrature to the random contributions. The dot-dashed line refers to the IR-resummed EFT model obtained by averaging c_0 over the 200 subsets. Finally, the bottom-right panel shows the reach of the models after approximately correcting the simulation data for the bias introduced by the finite mass resolution (see the main text for details). The shaded regions encompass the range of variability of the corrections while the solid lines are taken from the top-left panel and are given as a reference. All panels show three vertical lines indicating: (i) the volume of a redshift bin of width $\Delta z = 0.2$ centred at $z = 1$ for a Euclid-like survey (dashed); (ii) the total volume of the Eos simulations (dot-dashed); (iii) the volume of the PT-challenge simulations in Nishimichi et al. (2020, dotted). Measurements and models are compared using a bin width of $\Delta k = k_{\text{F}}$.

of models for P and B changes with the volume over which the measurements are performed. These plots are obtained as follows. (i) We pick a volume V which corresponds to an integer number N of MINERVA boxes. (ii) We randomly select N MINERVA realisations (with no repetitions) and compute $\langle \hat{P} \rangle$ and $\langle \hat{B} \rangle$ (using $\Delta k = k_{\text{F}}$ for P and $3 k_{\text{F}}$ for B in order to probe a wider range of scales). (iii) We fit the EFT counterterms to the numerical data using $k_{\text{fit}} = 0.14 h \text{ Mpc}^{-1}$ for P and $k_{\text{fit}} = 0.125 h \text{ Mpc}^{-1}$ for B . (iv) We evaluate the χ_{m}^2 statistic as a function of k_{\max} and use it to determine the

reach of each model based on the (one-sided) 95-per-cent confidence limits for the chi-squared distribution. (v) We repeat the procedure from step (ii) onward 200 times. (vi) We plot the median value of the reach (top-left panels) and its scatter (top-right panels) as a function of V .

In order to ease the interpretation of our results and facilitate comparison with the literature, we draw vertical lines marking three characteristic volumes. From left to right, they are: (i) $V = 7.94 h^{-3} \text{ Gpc}^3$ which corresponds to a redshift bin centred at

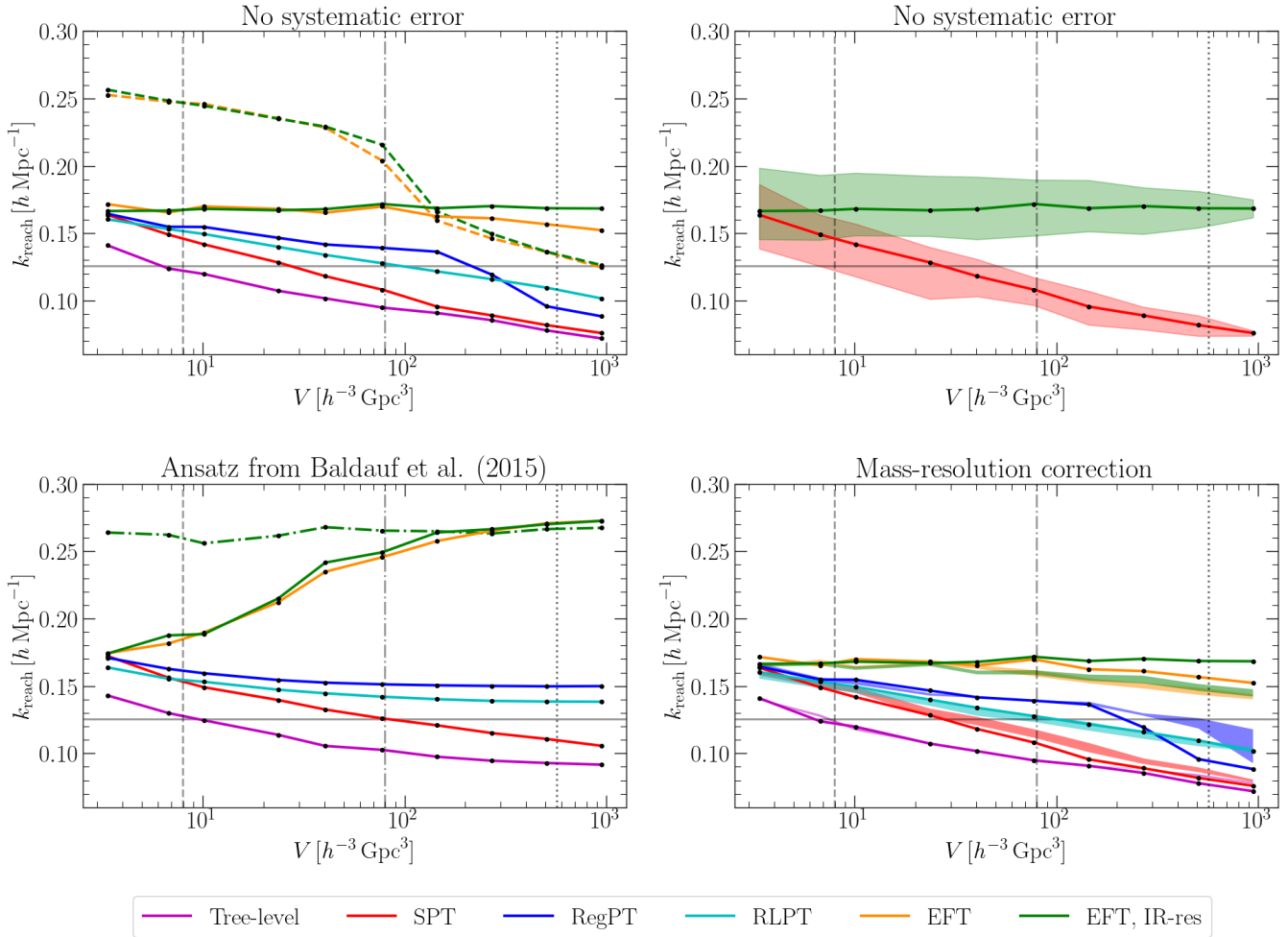


Figure 11. As in Fig. 10 but for the bispectrum models and using $\Delta k = 3 k_F$. In the bottom-left panel, systematic errors were added in quadrature to the statistical errors of the measurements following the ansatz of Baldauf et al. (2015c).

$z = 1$ and of width $\Delta z = 0.2$ of a Euclid-like survey (Euclid Collaboration et al. 2020); (ii) $V = 80 h^{-3} \text{ Gpc}^3$ which coincides with the total volume of the Eos simulations (and is approximately a factor 1.5 larger than the volume of the simulations used in Baldauf et al. 2015b,c; Steele & Baldauf 2021); (iii) $V = 566 h^{-3} \text{ Gpc}^3$ which is the volume of the simulation used in the blinded challenge paper of Nishimichi et al. (2020).

We are now ready to discuss the results presented in the top-left panels of Figs. 10 and 11. As expected, the domain of accuracy of the models decreases with increasing V . The only exception is the case of the EFT bispectrum for which the reach turns out to be independent of the simulation volume and corresponds to approximately $0.17 h \text{ Mpc}^{-1}$. The ranking of the models is pretty much independent of V , with SPT always being the first to break down and EFT the last. However, RegPT does better than RLPT for small V while the order is reversed for large V . It is also worth noticing that, while RegPT quite significantly extends the reach of SPT for the power spectrum for $V \approx 8 h^{-3} \text{ Gpc}^3$, it gives much smaller improvements for the bispectrum.

The nominal range of accuracy of EFT always extends beyond k_{fit} (indicated with horizontal grey lines in the figures). This is not surprising because, when the χ_m^2 statistic suggests a good fit at k_{fit} , our definition of the reach will automatically pick a larger

wavenumber. Essentially, what this means is that the EFT fits at k_{fit} are good (or even too good) in terms of χ_m^2 . We remind the reader that the values for k_{fit} we use are chosen in section 5.1 based on two criteria: (i) avoiding that the best-fitting EFT parameters run with k_{fit} and (ii) requiring consistency between the results obtained from P and B . However, since section 5.1 takes into consideration the full MINERVA set, our selected values might be considered ‘conservative’ when V is reduced (although we believe we should always perform the most challenging test for the theory, i.e. use the largest possible volume to test its basic assumptions like the scale-independence of the free parameters). For comparison, in the top-left panels of Figs. 10 and 11, we also show the range of accuracy one would obtain by fitting the EFT parameters up to $k_{\text{fit}} = 0.22 h \text{ Mpc}^{-1}$ (yellow and green dashed lines). This vastly increases the reach at small V (for both P and B) but reduces it at large V . In particular, for large enough volumes, the estimated reach becomes smaller than k_{fit} meaning that it is impossible to get a good fit to the numerical data.

So far we have concentrated on the median range of accuracy of each model. For this reason, in the top-right panels of Figs. 10 and 11, we plot the statistical uncertainty of the estimated reach as a function of V . In this case, we only consider SPT and IR-resummed EFT to improve readability. The shaded areas indicate the central

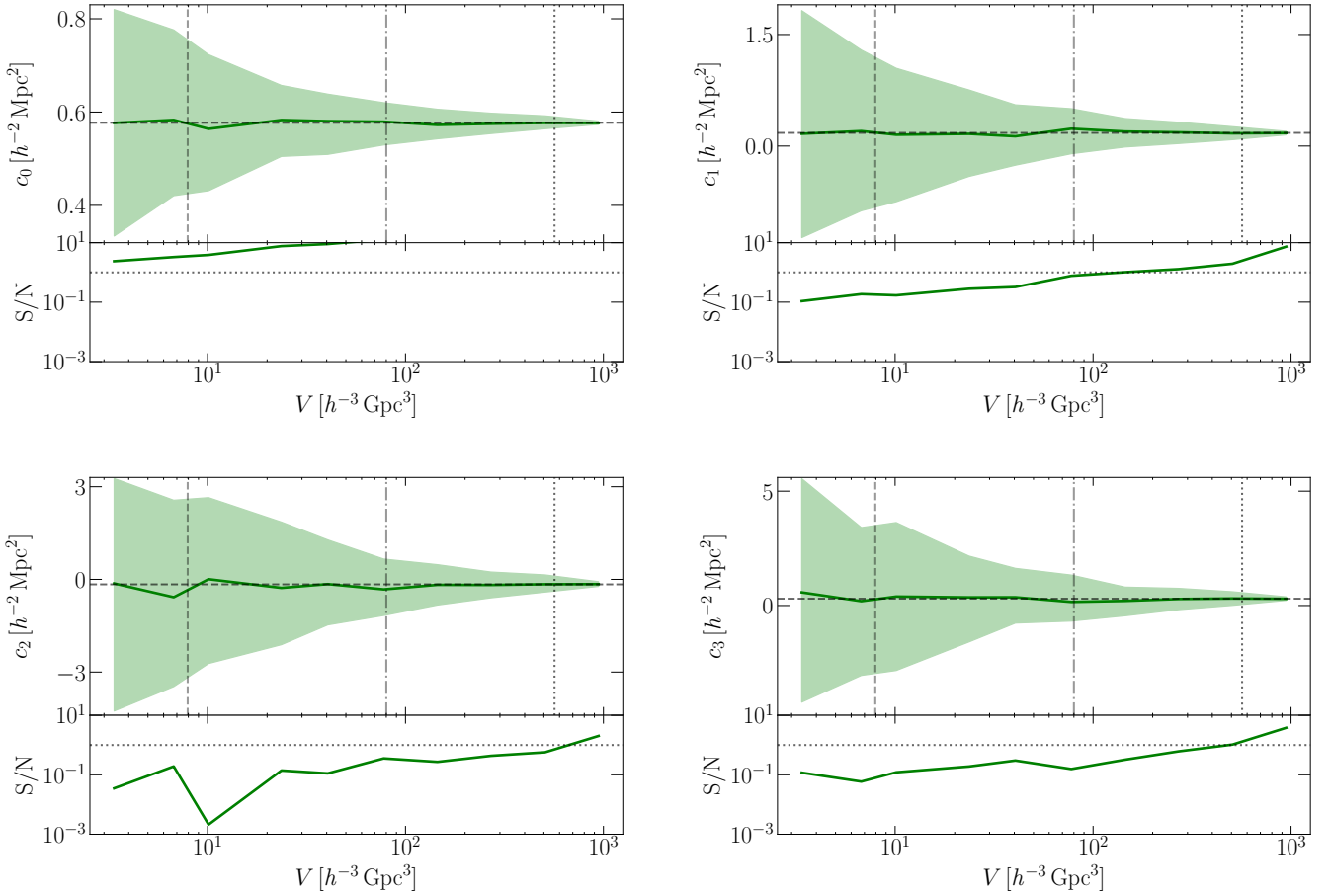


Figure 12. Distribution of the best-fitting EFT parameters as a function of the volume V used to measure the power spectrum and the bispectrum. The data refer to the counterterms of the IR-resummed EFT model with $k_{\text{fit}} = 0.125 h \text{ Mpc}^{-1}$. The parameter c_0 is derived from the power spectrum while c_1 , c_2 and c_3 are determined from the bispectrum. The top panels show the median (solid) and the central 68-per-cent region (shaded) over 200 realisations. The horizontal dashed lines indicate the values obtained from the full MINERVA simulation suite and given in Table 3. The three vertical lines mark the same volumes as in Figs. 10 and 11. The bottom panels show the signal-to-noise ratio defined as the ratio between the median and half the central 68-per-cent interval.

68-per-cent region⁵ among the 200 sets of simulations with volume V . It turns out that the error on the reach is by no means negligible, particularly for EFT which contains free parameters. It is therefore important to take this into account when comparing studies based on different simulations. In Fig. 12, we show how the distribution of the best-fitting amplitudes for the counterterms varies with V . We consider the IR-resummed EFT model for the bispectrum, fit c_0 from P and the other counterterms from B , and use $k_{\text{fit}} = 0.125 h \text{ Mpc}^{-1}$. It is important to notice that, while the median values of the EFT parameters approximately coincide with those in Table 3, the scatter around them strongly depends on V . For the redshift shell in a Euclid-like survey, c_1, c_2 and c_3 show a tremendous variability meaning that they cannot be accurately measured from a single realisation. In order to get a signal-to-noise ratio of order unity for them, it is necessary to consider volumes $V > 500 h^{-3} \text{ Gpc}^3$. As a means to further investigate the impact of the fitting strategy for the counterterms, in Fig. 13, we consider four methods in which the EFT parameters are determined in different ways as indicated in Table 4. For the full MINERVA data set, our standard choice

($1P+3B$) corresponds to the largest reach, while the one-parameter fit $1P+0B$ performs best for $V < 50 h^{-3} \text{ Gpc}^3$ suggesting that there is no need to use three counterterms when the surveyed volume is small and the error bars of the measurements are large. Angulo et al. (2015) reached similar conclusions using $V = 27 h^{-3} \text{ Gpc}^3$ and $k_{\text{fit}} = 0.1 h \text{ Mpc}^{-1}$ (conjecturing that the other counterterms give contributions comparable in size to two-loop corrections). In Fig. 13, there is nothing surprising about the fact that models with less free parameters can have a larger reach given that the EFT counterterms are determined using $k_{\text{fit}} = 0.125 h \text{ Mpc}^{-1}$ and the estimated reach is substantially larger than that. It is interesting to try to understand why it is preferable to set $c_1 = c_2 = c_3 = 0$ for small V . We believe that the reason is related to the fact that the expected values given in Table 3 are much smaller than the scatter seen in Fig. 12. Basically, the fit picks large ‘random’ counterterms in each realisation in order to adjust to the specific noise features.

In conclusion, the peculiarity of the EFT approach is the presence of free parameters in the counterterms that need to be determined from the measurements. Our results show that the methodology used to fix the EFT parameters heavily influences the range of accuracy of the theory. Basically, when the V is small, error bars are large, and the counterterms are poorly determined, the resulting freedom in the EFT parameters boosts the apparent reach of the

⁵ Obviously, this statistic underestimates the actual scatter when V approaches the total volume of the Minerva simulations as the different samples mostly overlap.

Method	c_0	c_1	c_2	c_3
$1P + 0B$	P	0	0	0
$1P + 3B$	P	B	B	B
$0P + 1B$	B	0	0	0
$0P + 4B$	B	B	B	B

Table 4. Schematic description of the methods used to fit the EFT counterterms in Fig. 13. The symbols P and B denote parameters determined by fitting (up to $k_{\text{fit}} = 0.125 h \text{ Mpc}^{-1}$) the power spectrum or the bispectrum, respectively. The number 0 indicates that the parameter is set to zero.

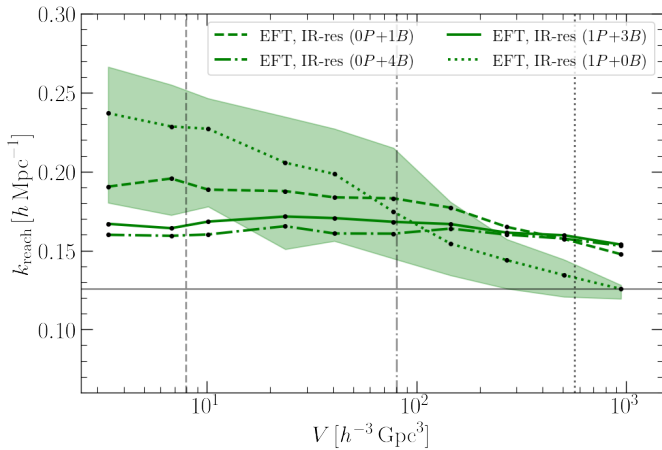


Figure 13. As in the top-left and top-right panels of Fig. 11 but for the IR-resummed EFT model with the counterterms determined as described in Table 4.

models. Care should then be taken to ensure that results from different studies are properly compared. Moreover, future studies should carefully investigate if and how the freedom in the counterterms impacts the estimation of cosmological parameters from the galaxy bispectrum that will be measured by the forthcoming generation of redshift surveys (Oddo et al. 2021).

5.5 Systematic errors

Just like any other numerical method, N -body simulations do not provide the exact solution to the problem of gravitational instability and perturbation growth. Modern codes are optimised based on a trade-off between computation speed and accuracy. Their finite mass and force resolution, the time-stepping criterion, the integration method, the way initial conditions are set and forces are computed generate small systematic deviations from the exact solution.

Several studies try to quantify the impact of these imperfections on various summary statistics (e.g. Takahashi et al. 2008; Nishimichi et al. 2009; Baldauf et al. 2015c; Schneider et al. 2016). However, the current understanding is not mature enough yet to provide a robust method for correcting goodness-of-fit statistics such as our χ_m^2 . Therefore, simplified approaches are necessary. The most elementary consists of adding small uncorrelated systematic errors to the statistical error budget. We follow this approach in the bottom-left panels of Figs. 10 and 11. For the power spectrum, we add a 0.5-per-cent systematic error in quadrature to the statistical error in order to approximately match the numerical results of Schneider et al. (2016). For the bispectrum, instead, we adopt two different

approaches. First, following Angulo et al. (2015), we consider a shape- and scale-independent systematic contribution at the 2-per-cent level (again summed in quadrature to the random error). As a second option, we use the scale-dependent ansatz by Baldauf et al. (2015c) which provides a fit to the systematic deviations measured among N -body simulations with different characteristics. In this case, the (relative) systematic error is

$$\frac{\Delta B}{B} = 0.01 + 0.02 \left(\frac{k_1}{0.5 h \text{ Mpc}^{-1}} \right), \quad (33)$$

where, as always, k_1 denotes the largest side of the triangular configuration. Since both approaches give very similar results, in Fig. 11 we only show those obtained with the scale-dependent ansatz. We are now ready to present our findings. For the models with no free-parameters, adding small systematic errors only changes the reach for large values of V , i.e. in every case in which the statistical errors are smaller than the additional systematic contributions. As a consequence, the resulting ranges of accuracy show little variations with V and RegPT turns out to consistently have the largest reach for all values of V . Conversely, the range of accuracy of EFT is strongly affected by the inclusion of systematic errors for all V . What is perhaps more surprising is that the reach of the EFT models increases with V . This happens because the values assigned to the EFT parameters scatter among the 200 subsets of simulations. In particular, when V is small, the EFT parameters have big uncertainties and the models cannot provide a good fit to the numerical data for large k_{max} . To clarify this further, we investigate what happens when we use the same EFT parameters for all simulation subsets. In this case, we use the mean of the values obtained from the individual sets. Our results are shown with dot-dashed lines in the bottom-left panels of Figs. 10 and 11. The reach for the power spectrum and bispectrum are extended to roughly 0.43 and 0.26 $h \text{ Mpc}^{-1}$, respectively, independently of V . Note, however, that the calibration of the EFT parameters without using the data is not doable in practical applications to observational surveys.

Systematic errors affect the accuracy and not the precision of measurements. Therefore, it is somewhat unnatural to model them as random uncorrelated errors. For example, it is well known that the finite mass resolution of N -body simulations leads to the suppression of density fluctuations on small scales (e.g. Heitmann et al. 2010; Schneider et al. 2016). In what follows, we propose a simple parameterisation of this effect which allows us to include it in our error budget as a ‘perfectly correlated’ error. Let us consider an N -body simulation with particle density \bar{n} and make the educated guess that, due to the finite mass resolution, $\delta_{\bar{n}}(\mathbf{k}) = \delta_{\infty}(\mathbf{k}) R_{\bar{n}}(k)$ where $\delta_{\infty}(\mathbf{k})$ denotes the ideal continuum case. It follows that

$$P_{\bar{n}}(k) = P_{\infty}(k) R_{\bar{n}}^2(k), \quad (34)$$

and

$$B_{\bar{n}}(k_1, k_2, k_3) = B_{\infty}(k_1, k_2, k_3) R_{\bar{n}}(k_1) R_{\bar{n}}(k_2) R_{\bar{n}}(k_3). \quad (35)$$

In order to constrain the shape of the function $R_{\bar{n}}(k)$ at $z = 1$, we use the power spectra extracted from 30 realisations of the Quijote simulations (Villaescusa-Navarro et al. 2020) at three different resolutions, i.e. using 256^3 , 512^3 and 1024^3 particles within a box of $1 h^{-3} \text{ Gpc}^3$. We find that the following parameterisation:

$$R_{\bar{n}}(k) = \frac{1}{1 + A(\bar{n}) \epsilon(k)} \quad (36)$$

with

$$\epsilon(k) = \frac{k}{h \text{ Mpc}^{-1}} + \alpha \left(\frac{k}{h \text{ Mpc}^{-1}} \right)^2 + \beta \left(\frac{k}{h \text{ Mpc}^{-1}} \right)^3, \quad (37)$$

accurately reproduces the numerical data up to $k_{\max} = 0.3 h \text{ Mpc}^{-1}$. The ratio between two power spectra obtained with different mass resolution is

$$\frac{P_{\bar{n}_1}(k)}{P_{\bar{n}_2}(k)} = \frac{R_{\bar{n}_1}^2(k)}{R_{\bar{n}_2}^2(k)} \simeq 1 + 2 \Delta A \epsilon(k), \quad (38)$$

where $\Delta A = A(\bar{n}_2) - A(\bar{n}_1)$ and we have Taylor expanded the final result to first order assuming that the corrections are small on the scales of interest. From the Quijote power spectra, we obtain $\alpha = -0.35$ and $\beta = 0.39$. In order to estimate $A(\bar{n}_{\text{MINERVA}})$, we assume that the correction is negligible at the highest Quijote resolution and interpolate ΔA (note that $\bar{n}_{\text{MINERVA}} = 0.296 h^3 \text{ Mpc}^{-3}$ while the Quijote simulations have $\bar{n} = 0.017, 0.134, \text{ and } 1.074 h^3 \text{ Mpc}^{-3}$). We obtain $A(\bar{n}_{\text{MINERVA}}) = 0.0188$ which corresponds to sub-percent corrections over all scales of interest. Eventually, we write the systematic error (bias) in the summary statistics extracted from an N -body simulation as

$$\Delta P = P_{\bar{n}} - P_{\infty} = P_{\bar{n}} \left(1 - \frac{1}{R_{\bar{n}}^2(k)} \right) \approx -2 P_{\bar{n}} A(\bar{n}) \epsilon(k), \quad (39)$$

$$\Delta B = B_{\bar{n}} - B_{\infty} \approx -B_{\bar{n}} A(\bar{n}) [\epsilon(k_1) + \epsilon(k_2) + \epsilon(k_3)]. \quad (40)$$

In order to apply this result to the MINERVA simulations we re-scale our estimate for $A(\bar{n}_{\text{MINERVA}})$ by a factor γ for which we consider three possible values, namely 0.5, 1.0 and 1.5. Although these values may not exactly describe the correction due to the finite mass resolution in the MINERVA runs, they allow us to conceptually investigate the effect of a scale- and shape-dependent bias. We thus re-compute the χ_m^2 statistic after shifting the measurements from the simulations according to the corrections given in equations (39) and (40). Our results for the reach of the models are displayed in the bottom-right panels of Figs. 10 and 11 where the coloured bands indicate the range of variability induced by γ and the solid lines reproduce the curves from the top-left panel to emphasize changes. Overall, the impact of the corrections is rather minor. Nonetheless, a few changes are worth noticing. For the power spectrum, the IR-resummed EFT at intermediate volumes shows the most marked improvement. For the bispectrum, accounting for the bias improves the reach of RegPT for large V and deteriorates it for both EFT models. Perhaps, the most important conclusion that one can draw from this test is that its results are very different from those obtained by simply inflating the random errors to account for systematics (as routinely done in the literature). The latter approach, in fact, artificially boosts the reach of models with free parameters as in the case of EFT. Our study calls for a better understanding of random and systematic errors in N -body simulations.

6 SUMMARY

Perturbative techniques based on fluid dynamics are widely used to study the growth of the large-scale structure of the Universe. In fact, they often are the only method of obtaining predictions with analytical control. The convergence properties of perturbation theory are still a matter of debate but there is mounting evidence that the resulting expressions for large-scale observables are actually asymptotic, i.e. only the truncated series expansion (including just the first few terms) provides an accurate approximation to the exact solution (e.g. Pajer & van der Woude 2018; Konstandin et al. 2019, and references therein).

Modern perturbative approaches come in a plethora of flavours and sometimes contain free parameters. It is thus imperative to

identify their regime of validity and accuracy before applying them to practical situations. N -body simulations of collisionless dark matter in a cosmological background are the standard test bed for inferring the reach of the different models.

The purpose of this study is threefold. First, we use a very large set of N -body simulations (the MINERVA suite) to test the NLO expansions for the matter power spectrum and bispectrum in five different implementations of perturbation theory, namely SPT, RegPT, RLPT, EFT and IR-resummed EFT. Second, we try to draw the line that demarcates general results from those affected by the method used to determine the reach of the models with free parameters (i.e. EFT and IR-resummed EFT). Third, we explore a novel way to account for the systematic errors introduced by the finite mass resolution of N -body simulations.

Specifically, we study how well the different models match the measurements from the simulations as a function of the maximum wavenumber considered, k_{\max} . Having in mind the forthcoming generation of surveys such as those that will be conducted by DESI and the Euclid mission, we only consider data at $z = 1$. We define the reach of a model as the minimum k_{\max} at which the χ^2 goodness-of-fit test rejects the null hypothesis that the N -body data are consistent with the model predictions at the significance level of 0.05. This requires making some assumptions about the covariance matrix of the measurements. We use the Gaussian approximation given in equation (25) for the power spectrum and a more sophisticated expression for the bispectrum – see equation (27). In both cases, we use a dedicated version of the χ^2 test to verify that these expressions closely approximate the covariance matrix of the measurements extracted from the simulations.

In the first part of our study, we consider the full MINERVA suite and neglect systematic errors in the simulations. Our main findings are as follows.

(i) By fitting the EFT parameters that determine the amplitude of the counterterms to the simulation data as a function of k_{\max} , we find that they remain stable until a maximum wavenumber and change beyond that (Figs. 3 and 4). The stability region ends at $k_{\max} = 0.14 h \text{ Mpc}^{-1}$ for the power spectrum and $0.125 h \text{ Mpc}^{-1}$ for the bispectrum. We use these values to define the default range of scales ($k < k_{\text{fit}}$) over which we fit the EFT parameters.

(ii) The χ^2 goodness-of-fit test for the power spectrum (Fig. 5) shows that EFT and IR-resummed EFT accurately match the simulations up to $k_{\max} = 0.14 h \text{ Mpc}^{-1}$ while all the models without free parameters fail at much larger scales, i.e. $k_{\max} = 0.06 h \text{ Mpc}^{-1}$.

(iii) Repeating the test for the bispectrum (Fig. 7) provides a clear ranking for the models based on their reach. The EFT models have the largest range of accuracy ($k_{\max} \simeq 0.16 - 0.19 h \text{ Mpc}^{-1}$, depending on the binning of the data) followed by RegPT and RLPT ($k_{\max} \simeq 0.10 - 0.14 h \text{ Mpc}^{-1}$) and SPT ($k_{\max} \simeq 0.08 h \text{ Mpc}^{-1}$). Note that the nominal reach of EFT extends beyond k_{fit} , meaning that the model with the counterterms fixed using triangle configurations with $k < k_{\text{fit}} = 0.125 h \text{ Mpc}^{-1}$ continues to provide a good fit on (slightly) smaller scales.

Next, by sub-sampling the MINERVA suite, we investigate how the reach of the models depends on the total volume covered by the simulations used in our tests. This is particularly useful when comparing different results in the literature and also to gauge the range of scales that can be robustly probed in an actual galaxy redshift survey. In this analysis, we approximately account for systematic effects introduced by the N -body technique using different methods. Our key results are as follows.

(iv) Obviously, the reach of the models improves for smaller volumes as the statistical error bars become larger and it is eas-

ier to fit the data. Considering a redshift bin of width $\Delta z = 0.2$ centred at $z = 1$ for a Euclid-like survey, gives a median reach for SPT of approximately $0.12 h \text{ Mpc}^{-1}$ for the power spectrum and $0.15 h \text{ Mpc}^{-1}$ for the bispectrum. On the other hand, for IR-resummed EFT we obtain $0.25 h \text{ Mpc}^{-1}$ for the power spectrum and $0.18 h \text{ Mpc}^{-1}$ for the bispectrum. All the other models lie in between these extremes (Figs. 10 and 11). It is also important to mention that the scatter of the reach between different realisations with the same volume becomes rather large for the models that have free parameters (the central 68-per-cent range for EFT extends from 0.19 to $0.34 h \text{ Mpc}^{-1}$ in the case of the power spectrum). This should be taken into account when comparing results from different studies.

(v) The estimated range of accuracy of the EFT predictions is heavily influenced by the procedure adopted to fit the counterterms. For the volume of the Euclid-like shell, using $k_{\text{fit}} = 0.22 h \text{ Mpc}^{-1}$ extends the median reach of the IR-resummed EFT model to 0.33 and $0.25 h \text{ Mpc}^{-1}$ for the power spectrum and the bispectrum, respectively, but degrades it for the full MINERVA set. For the bispectrum, fitting only c_0 from the power spectrum and setting the other three counterterms to zero gives the largest reach for $V < 100 h^{-3} \text{ Mpc}^3$. Fitting all the four parameters is instead preferred for larger volumes (Fig. 13). Therefore, it is difficult to unequivocally define a reach for the models with free parameters.

(vi) The results above are only slightly affected (less than 10 per cent change) by accounting for a scale- and shape-dependent bias due to the finite mass resolution of the N -body simulations.

(vii) The situation is very different when uncorrelated systematic errors are added in quadrature to the statistical uncertainties, as assumed in Baldauf et al. (2015c) and Angulo et al. (2015). In this case, the reach of EFT is dramatically extended thanks to the freedom provided by the counterterms. For example, considering the whole MINERVA suite, we obtain that the IR-resummed EFT model provides a good fit until 0.40 and $0.27 h \text{ Mpc}^{-1}$ for the power-spectrum and the bispectrum, respectively. More modest changes are seen for the models with no fixed parameters at large V .

In order to constrain the cosmological parameters from the galaxy bispectrum, it is necessary to model galaxy biasing, discreteness effects, and redshift-space distortions on top of the nonlinearities of the matter density field. It is very well possible that the additional terms in the expressions for the galaxy bispectrum to NLO will be degenerate with higher-order terms in the matter models and thus extend the reach of the more complex mathematical descriptions beyond the scales determined in this work. Yet, it is pivotal to retain control over the extent to which this is happening, especially if one wants to assign a physical meaning to the additional (e.g. bias and shot-noise) parameters. This is why we believe our work is important.

ACKNOWLEDGEMENTS

We are grateful to Claudio Dalla Vecchia and Ariel Sanchez for running and making available the MINERVA simulations, performed and analysed on the Hydra and Euclid clusters at the Max Planck Computing and Data Facility (MPCDF) in Garching. We thank Martin Crocce, Alex Eggemeier, Azadeh Moradinezhad, Roman Scoccimarro and Zvonimir Vlah for useful discussions. We acknowledge the hospitality of the Institute for Fundamental Physics of the Universe in Trieste where part of this work was carried out in October 2019. D.A. acknowledges partial financial support by the Shota Rustaveli National Science Foundation of Georgia (GNSF) under the

grant FR-19-498. E.S. is partially supported by the INFN INDARK PD51 grant and acknowledges support from PRIN MIUR 2015 Cosmology and Fundamental Physics: illuminating the Dark Universe with Euclid. M.B. acknowledges support from the Netherlands Organization for Scientific Research (NWO), which is funded by the Dutch Ministry of Education, Culture and Science (OCW), under VENI grant 016.Veni.192.210. M.B. also acknowledges support from the NWO under the project ‘‘Cosmic Origins from Simulated Universes’’ for the computing time allocated to run a subset of the Eos Simulations on CARTESIUS, a supercomputer which is part of the Dutch National Computing Facilities. A.L. acknowledges funding by the LabEx ENS-ICFP: ANR-10-LABX-0010/ANR-10-IDEX-0001-02 PSL*. V.Y. acknowledges funding from the European Research Council (ERC) under the European Union’s Horizon 2020 research and innovation programme (grant agreement No 769130).

DATA AVAILABILITY

The data underlying this article will be shared on reasonable request to the corresponding author.

REFERENCES

- Agarwal N., Desjacques V., Jeong D., Schmidt F., 2021, *J. Cosmology Astropart. Phys.*, 2021, 021
- Angulo R. E., Foreman S., Schmittfull M., Senatore L., 2015, *J. Cosmology Astropart. Phys.*, 10, 039
- Baldauf T., Mirbabayi M., Simonović M., Zaldarriaga M., 2015a, *Phys. Rev. D*, 92, 043514
- Baldauf T., Mergolli L., Zaldarriaga M., 2015b, *Phys. Rev. D*, 92, 123007
- Baldauf T., Mergolli L., Mirbabayi M., Pajer E., 2015c, *J. Cosmology Astropart. Phys.*, 2015, 007
- Baldauf T., Mirbabayi M., Simonović M., Zaldarriaga M., 2016, arXiv e-prints, p. arXiv:1602.00674
- Barreira A., 2020, *J. Cosmology Astropart. Phys.*, 2020, 031
- Baumann D., Nicolis A., Senatore L., Zaldarriaga M., 2012, *J. Cosmology Astropart. Phys.*, 2012, 051
- Bernardeau F., Colombi S., Gaztañaga E., Scoccimarro R., 2002, *Phys. Rep.*, 367, 1
- Bernardeau F., Crocce M., Scoccimarro R., 2008, *Phys. Rev. D*, 78, 103521
- Bernardeau F., Crocce M., Scoccimarro R., 2012, *Phys. Rev. D*, 85, 123519
- Biagetti M., Lazeyras T., Baldauf T., Desjacques V., Schmidt F., 2017, *MNRAS*, 468, 3277
- Blas D., Lesgourgues J., Tram T., 2011, *J. Cosmology Astropart. Phys.*, 2011, 034
- Blas D., Garny M., Konstandin T., 2014, *J. Cosmology Astropart. Phys.*, 2014, 010
- Blas D., Garny M., Ivanov M. M., Sibiryakov S., 2016, *J. Cosmology Astropart. Phys.*, 2016, 028
- Carlson J., White M., Padmanabhan N., 2009, *Phys. Rev. D*, 80, 043531
- Carlson J., Reid B., White M., 2013, *MNRAS*, 429, 1674
- Carrasco J. J. M., Hertzberg M. P., Senatore L., 2012, *Journal of High Energy Physics*, 2012, 82
- Carrasco J. J. M., Foreman S., Green D., Senatore L., 2014a, *J. Cosmology Astropart. Phys.*, 7, 56
- Carrasco J. J. M., Foreman S., Green D., Senatore L., 2014b, *J. Cosmology Astropart. Phys.*, 7, 57
- Catelan P., 1995, *MNRAS*, 276, 115
- Chan K. C., Blot L., 2017, *Phys. Rev. D*, 96, 023528
- Chudaykin A., Ivanov M. M., 2019, *J. Cosmology Astropart. Phys.*, 2019, 034
- Chudaykin A., Ivanov M. M., Simonović M., 2021, *Phys. Rev. D*, 103, 043525
- Colavincenzo M., et al., 2019, *MNRAS*, 482, 4883

- Cole S., et al., 2005, *MNRAS*, **362**, 505
- Crocce M., Scoccimarro R., 2006a, *Phys. Rev. D*, **73**, 063519
- Crocce M., Scoccimarro R., 2006b, *Phys. Rev. D*, **73**, 063520
- Crocce M., Scoccimarro R., 2008, *Phys. Rev. D*, **77**, 023533
- Crocce M., Pueblas S., Scoccimarro R., 2006, *MNRAS*, **373**, 369
- Crocce M., Scoccimarro R., Bernardeau F., 2012, *MNRAS*, **427**, 2537
- DESI Collaboration et al., 2016, arXiv e-prints, p. arXiv:1611.00036
- Eggemeier A., Scoccimarro R., Smith R. E., Crocce M., Pezzotta A., Sánchez A. G., 2021, arXiv e-prints, p. arXiv:2102.06902
- Euclid Collaboration et al., 2020, *A&A*, **642**, A191
- Feldman H. A., Kaiser N., Peacock J. A., 1994, *ApJ*, **426**, 23
- Fisher K. B., Nusser A., 1996, *MNRAS*, **279**, L1
- Foreman S., Senatore L., 2016, *J. Cosmology Astropart. Phys.*, **2016**, 033
- Foreman S., Perrier H., Senatore L., 2016, *J. Cosmology Astropart. Phys.*, **2016**, 027
- Fry J. N., 1984, *ApJ*, **279**, 499
- Gaztañaga E., Norberg P., Baugh C. M., Croton D. J., 2005, *MNRAS*, **364**, 620
- Gaztanaga E., 1994, *MNRAS*, **268**, 913
- Gil-Marín H., Noreña J., Verde L., Percival W. J., Wagner C., Manera M., Schneider D. P., 2015a, *MNRAS*, **451**, 539
- Gil-Marín H., et al., 2015b, *MNRAS*, **452**, 1914
- Gil-Marín H., Percival W. J., Verde L., Brownstein J. R., Chuang C.-H., Kitaura F.-S., Rodríguez-Torres S. A., Olmstead M. D., 2017, *MNRAS*, **465**, 1757
- Goroff M. H., Grinstein B., Rey S. J., Wise M. B., 1986, *ApJ*, **311**, 6
- Grieb J. N., Sánchez A. G., Salazar-Albornoz S., Dalla Vecchia C., 2016, *MNRAS*, **457**, 1577
- Gualdi D., Verde L., 2020, *J. Cosmology Astropart. Phys.*, **2020**, 041
- Gualdi D., Gil-Marín H., Manera M., Joachimi B., Lahav O., 2019, *MNRAS*, **484**, L29
- Hahn C., Villaescusa-Navarro F., 2021, *J. Cosmology Astropart. Phys.*, **2021**, 029
- Heinrich C., Doré O., 2020, *Phys. Rev. D*, **102**, 123549
- Heitmann K., White M., Wagner C., Habib S., Higdon D., 2010, *ApJ*, **715**, 104
- Hertzberg M. P., 2014, *Phys. Rev. D*, **89**, 043521
- Howlett C., Lewis A., Hall A., Challinor A., 2012, *J. Cosmology Astropart. Phys.*, **2012**, 027
- Ivanov M. M., Sibiryakov S., 2018, *J. Cosmology Astropart. Phys.*, **2018**, 053
- Ivanov M. M., Simonović M., Zaldarriaga M., 2020, *J. Cosmology Astropart. Phys.*, **2020**, 042
- Konstantin T., Porto R. A., Rubira H., 2019, *J. Cosmology Astropart. Phys.*, **2019**, 027
- Kulkarni G. V., Nichol R. C., Sheth R. K., Seo H.-J., Eisenstein D. J., Gray A., 2007, *MNRAS*, **378**, 1196
- Laureijs R., et al., 2011, arXiv e-prints, p. arXiv:1110.3193
- Lazanu A., Giannantonio T., Schmittfull M., Shellard E. P. S., 2016, *Phys. Rev. D*, **93**, 083517
- Lewis A., Challinor A., Lasenby A., 2000, *ApJ*, **538**, 473
- Matarrese S., Pietroni M., 2007, *J. Cosmology Astropart. Phys.*, **2007**, 026
- Matsubara T., 2008, *Phys. Rev. D*, **77**, 063530
- McBride C. K., Connolly A. J., Gardner J. P., Scranton R., Newman J. A., Scoccimarro R., Zehavi I., Schneider D. P., 2011, *ApJ*, **726**, 13
- Meiksin A., White M., 1999, *MNRAS*, **308**, 1179
- Meiksin A., White M., Peacock J. A., 1999, *MNRAS*, **304**, 851
- Moradinezhad Dizgah A., Biagetti M., Sefusatti E., Desjacques V., Noreña J., 2021, *J. Cosmology Astropart. Phys.*, **2021**, 015
- Moutarde F., Alimi J. M., Bouchet F. R., Pellat R., Ramani A., 1991, *ApJ*, **382**, 377
- Nishimichi T., et al., 2009, *PASJ*, **61**, 321
- Nishimichi T., D'Amico G., Ivanov M. M., Senatore L., Simonović M., Takada M., Zaldarriaga M., Zhang P., 2020, *Phys. Rev. D*, **102**, 123541
- Oddo A., Sefusatti E., Porciani C., Monaco P., Sánchez A. G., 2020, *J. Cosmology Astropart. Phys.*, **2020**, 056
- Oddo A., Rizzo F., Sefusatti E., Porciani C., 2021, *in prep.*
- Osato K., Nishimichi T., Bernardeau F., Taruya A., 2019, *Phys. Rev. D*, **99**, 063530
- Pajer E., van der Woude D., 2018, *J. Cosmology Astropart. Phys.*, **2018**, 039
- Pan J., Szapudi I., 2005, *MNRAS*, **362**, 1363
- Pearson D. W., Samushia L., 2018, *MNRAS*, **478**, 4500
- Peebles P. J. E., Groth E. J., 1975, *ApJ*, **196**, 1
- Pietroni M., 2008, *J. Cosmology Astropart. Phys.*, **2008**, 036
- Porciani C., 2021, *in prep.*
- Porto R. A., Senatore L., Zaldarriaga M., 2014, *J. Cosmology Astropart. Phys.*, **5**, 22
- Pueblas S., Scoccimarro R., 2009, *Phys. Rev. D*, **80**, 043504
- Rampf C., Wong Y. Y. Y., 2012, *J. Cosmology Astropart. Phys.*, **6**, 18
- Roth N., Porciani C., 2011, *MNRAS*, **415**, 829
- Samushia L., Slepian Z., Villaescusa-Navarro F., 2021, *MNRAS*, **505**, 628
- Schneider A., et al., 2016, *J. Cosmology Astropart. Phys.*, **2016**, 047
- Scoccimarro R., 1997, *ApJ*, **487**, 1
- Scoccimarro R., Colombi S., Fry J. N., Frieman J. A., Hivon E., Melott A., 1998, *Astrophys. J.*, **496**, 586
- Scoccimarro R., Feldman H. A., Fry J. N., Frieman J. A., 2001, *ApJ*, **546**, 652
- Sefusatti E., Scoccimarro R., 2005, *Phys. Rev. D*, **71**, 063001
- Sefusatti E., Crocce M., Pueblas S., Scoccimarro R., 2006, *Phys. Rev. D*, **74**, 023522
- Sefusatti E., Crocce M., Desjacques V., 2010, *MNRAS*, **406**, 1014
- Sefusatti E., Crocce M., Scoccimarro R., Couchman H. M. P., 2016, *MNRAS*, **460**, 3624
- Senatore L., Zaldarriaga M., 2015, *J. Cosmology Astropart. Phys.*, **2015**, 013
- Slepian Z., et al., 2017a, *MNRAS*, **468**, 1070
- Slepian Z., et al., 2017b, *MNRAS*, **469**, 1738
- Slepian Z., et al., 2018, *MNRAS*, **474**, 2109
- Springel V., 2005, *MNRAS*, **364**, 1105
- Steele T., Baldauf T., 2021, *Phys. Rev. D*, **103**, 023520
- Takahashi R., 2008, *Progress of Theoretical Physics*, **120**, 549
- Takahashi R., et al., 2008, *MNRAS*, **389**, 1675
- Taruya A., Nishimichi T., Saito S., Hiramatsu T., 2009, *Phys. Rev. D*, **80**, 123503
- Taruya A., Bernardeau F., Nishimichi T., Codis S., 2012, *Phys. Rev. D*, **86**, 103528
- Taruya A., Nishimichi T., Jeong D., 2018, *Phys. Rev. D*, **98**, 103532
- Taylor A. N., Hamilton A. J. S., 1996, *MNRAS*, **282**, 767
- Verde L., et al., 2002, *MNRAS*, **335**, 432
- Villaescusa-Navarro F., et al., 2020, *ApJS*, **250**, 2
- Vlah Z., Seljak U., Yat Chu M., Feng Y., 2016, *J. Cosmology Astropart. Phys.*, **2016**, 057
- Yankelevich V., Porciani C., 2019, *MNRAS*, **483**, 2078
- Zel'dovich Y. B., 1970, *A&A*, **5**, 84
- d'Amico G., Gleyzes J., Kokron N., Markovic K., Senatore L., Zhang P., Beutler F., Gil-Marín H., 2020, *J. Cosmology Astropart. Phys.*, **2020**, 005

APPENDIX A: SPT

The one-loop correction to the matter power spectrum in SPT is

$$P_{\text{SPT}}^{1\text{-loop}}(k, z) = P_{13}(k, z) + P_{22}(k, z), \quad (\text{A1})$$

where

$$P_{13}(k, z) = 6 [D(z)]^4 P_L(k) \int_{\mathbf{q}} F_2(\mathbf{k}, \mathbf{q}, -\mathbf{q}) P_L(q), \quad (\text{A2})$$

$$P_{22}(k, z) = 2 [D(z)]^4 \int_{\mathbf{q}} [F_2(\mathbf{q}, \mathbf{k} - \mathbf{q})]^2 P_L(|\mathbf{k} - \mathbf{q}|) P_L(q), \quad (\text{A3})$$

and $\int_{\mathbf{q}}$ denotes $\int \frac{d^3\mathbf{q}}{(2\pi)^3}$.

Similarly, for the bispectrum, we have:

$$B_{\text{SPT}}^{1\text{-loop}} = B_{222} + B_{321}^I + B_{321}^{II} + B_{411}, \quad (\text{A4})$$

with

$$B_{222}(k_1, k_2, k_3, z) = 8 [D(z)]^6 \int_{\mathbf{q}} P_L(q) P_L(|\mathbf{k}_2 - \mathbf{q}|) P_L(|\mathbf{k}_3 + \mathbf{q}|) \\ \times F_2(-\mathbf{q}, \mathbf{k}_3 + \mathbf{q}) F_2(\mathbf{k}_3 + \mathbf{q}, \mathbf{k}_2 - \mathbf{q}) F_2(\mathbf{k}_2 - \mathbf{q}, \mathbf{q}) \quad (\text{A5})$$

$$B_{321}^I(k_1, k_2, k_3, z) = 6 [D(z)]^6 P_L(k_3) \int_{\mathbf{q}} P_L(|\mathbf{k}_2 - \mathbf{q}|) P_L(q) \\ \times F_3(-\mathbf{q}, -\mathbf{k}_2 + \mathbf{q}, -\mathbf{k}_3) F_2(\mathbf{k}_2 - \mathbf{q}, \mathbf{q}) + 5 \text{ perms.} \quad (\text{A6})$$

$$B_{321}^{II}(k_1, k_2, k_3, z) = 6 [D(z)]^6 P_L(k_2) P_L(k_3) F_2^{(s)}(\mathbf{k}_2, \mathbf{k}_3) \\ \times \int_{\mathbf{q}} P_L(q) F_3(\mathbf{k}_3, \mathbf{q}, -\mathbf{q}) + 5 \text{ perms.} \quad (\text{A7})$$

$$B_{411}(k_1, k_2, k_3, z) = 12 [D(z)]^6 (z) P_L(k_2) P_L(k_3) \\ \times \int_{\mathbf{q}} P_L(q) F_4(\mathbf{q}, -\mathbf{q}, -\mathbf{k}_2, -\mathbf{k}_3) + 2 \text{ perms.} \quad (\text{A8})$$

APPENDIX B: REGPT

The $(p+1)$ -point propagator, $\Gamma^{(p)}(\mathbf{k}_1, \dots, \mathbf{k}_p, z)$, is defined as

$$\frac{1}{p!} \left\langle \frac{\delta^p \delta(\mathbf{k}, z)}{\delta \delta_L(\mathbf{k}_1) \dots \delta \delta_L(\mathbf{k}_p)} \right\rangle = \frac{\delta_D(\mathbf{k} - \mathbf{k}_{1\dots p})}{(2\pi)^{3(p-1)}} \Gamma^{(p)}, \quad (\text{B1})$$

and can be expanded using equations (4) and (B1) as

$$\Gamma^{(p)} = \Gamma_{\text{tree}}^{(p)} + \sum_{n=1}^{\infty} \Gamma_{n\text{-loop}}^{(p)}. \quad (\text{B2})$$

$\Gamma_{\text{tree}}^{(p)}(\mathbf{k}_1, \dots, \mathbf{k}_p, z) = [D(z)]^p F_p(\mathbf{k}_1, \dots, \mathbf{k}_p)$ and

$$\Gamma_{n\text{-loop}}^{(p)}(\mathbf{k}_1, \dots, \mathbf{k}_p, z) = [D(z)]^{(2n+p)} C_p^{2n+p} (2n-1)!! \\ \times \int \frac{d^3 \mathbf{q}_1 \dots d^3 \mathbf{q}_n}{(2\pi)^{3n}} F_{2n+p}(\mathbf{q}_1, -\mathbf{q}_1, \dots, \mathbf{q}_n, -\mathbf{q}_n, \mathbf{k}_1, \dots, \mathbf{k}_p) \\ \times P_L(q_1) \dots P_L(q_n) \equiv [D(z)]^{(2n+p)} \bar{\Gamma}_{n\text{-loop}}^{(p)}(\mathbf{k}_1, \dots, \mathbf{k}_p), \quad (\text{B3})$$

where C_p^{2n+p} denotes the binomial coefficient. Resumming the subset of terms that provide the dominant contribution at small scales gives (Crocce & Scoccimarro 2006b; Bernardeau et al. 2008)

$$\Gamma^{(p)}(\mathbf{k}_1, \dots, \mathbf{k}_p, z) \xrightarrow{k \rightarrow \infty} \exp \left\{ -\frac{k^2 [D(z)]^2 \sigma_d^2}{2} \right\} \Gamma_{\text{tree}}^{(p)}. \quad (\text{B4})$$

where

$$\sigma_d^2 = \frac{1}{3} \int \frac{d^3 \mathbf{q}}{(2\pi)^3} \frac{P_L(q)}{q^2} \quad (\text{B5})$$

is the rms value of the one-dimensional linear displacement field. Up to one-loop order, the regularized propagators which interpolate between the two asymptotic regimes are (Taruya et al. 2012; Bernardeau et al. 2012)

$$\Gamma_{\text{reg}}^{(1)}(k, z) = D(z) \left\{ 1 + \frac{k^2 [D(z)]^2 \sigma_d^2}{2} + [D(z)]^2 \bar{\Gamma}_{1\text{-loop}}^{(1)}(k) \right\} \\ \times \exp \left\{ -\frac{k^2 [D(z)]^2 \sigma_d^2}{2} \right\} \quad (\text{B6})$$

$$\Gamma_{\text{reg}}^{(2)}(\mathbf{k}_1, \mathbf{k}_2, z) = [D(z)]^2 \left(F_2(\mathbf{k}_1, \mathbf{k}_2) \left\{ 1 + \frac{k^2 [D(z)]^2 \sigma_d^2}{2} \right\} \right. \\ \left. + [D(z)]^2 \bar{\Gamma}_{1\text{-loop}}^{(2)}(\mathbf{k}_1, \mathbf{k}_2) \right) \exp \left\{ -\frac{k^2 [D(z)]^2 \sigma_d^2}{2} \right\}, \quad (\text{B7})$$

$$\Gamma_{\text{reg}}^{(3)}(\mathbf{k}_1, \mathbf{k}_2, \mathbf{k}_3, z) = [D(z)]^3 F_3(\mathbf{k}_1, \mathbf{k}_2, \mathbf{k}_3) \\ \times \exp \left\{ -\frac{k^2 [D(z)]^2 \sigma_d^2}{2} \right\}. \quad (\text{B8})$$

In this formalism, the matter power spectrum and bispectrum up to one-loop corrections can be expressed as (Bernardeau et al. 2008)

$$P(k, z) = [\Gamma^{(1)}(k, z)]^2 P_L(k) \\ + 2 \int_{\mathbf{q}} [\Gamma^{(2)}(\mathbf{q}, \mathbf{k} - \mathbf{q}, z)]^2 P_L(q) P_L(|\mathbf{k} - \mathbf{q}|), \quad (\text{B9})$$

$$B(\mathbf{k}_1, \mathbf{k}_2, \mathbf{k}_3, z) = 2 \Gamma^{(2)}(\mathbf{k}_1, \mathbf{k}_2, z) \Gamma^{(1)}(k_1, z) \Gamma^{(1)}(k_2, z) \\ \times P_L(k_1) P_L(k_2) + 2 \text{ perms.} \\ + \left[8 \int_{\mathbf{q}} \Gamma^{(2)}(\mathbf{k}_1 + \mathbf{q}, -\mathbf{q}, z) \Gamma^{(2)}(-\mathbf{k}_1 - \mathbf{q}, \mathbf{q} - \mathbf{k}_2, z) \right. \\ \times \Gamma^{(2)}(\mathbf{k}_2 - \mathbf{q}, \mathbf{q}, z) P_L(|\mathbf{k}_2 - \mathbf{q}|) P_L(|\mathbf{k}_1 + \mathbf{q}|) P_L(q) \left. \right] \\ + \left[6 \Gamma^{(1)}(\mathbf{k}_3, z) P_L(k_3) \int_{\mathbf{q}} \Gamma^{(3)}(\mathbf{q} - \mathbf{k}_2, -\mathbf{k}_3, -\mathbf{q}, z) \right. \\ \times \Gamma^{(2)}(\mathbf{q}, \mathbf{k}_2 - \mathbf{q}, z) P_L(|\mathbf{k}_2 - \mathbf{q}|) P_L(q) + 5 \text{ perms.} \left. \right]. \quad (\text{B10})$$

APPENDIX C: RLPT

By combining the Lagrangian perturbative expansion with equations (9) and (10), one obtains the following expressions at one loop (Matsubara 2008; Rampf & Wong 2012):

$$P_{\text{RLPT}}(k) = \left[P_L + P_{\text{SPT}}^{1\text{-loop}} + \frac{k^2}{6\pi^2} P_L \int dq P_L(q) \right] \\ \times \exp \left[-\frac{k^2}{6\pi^2} \int dq P_L(q) \right], \quad (\text{C1})$$

$$B_{\text{RLPT}}(k_1, k_2, k_3) = \left[B_{\text{SPT}}^{\text{tree}} \left\{ 1 + \frac{k_1^2 + k_2^2 + k_3^2}{12\pi^2} \int dq P_L(q) \right\} \right. \\ \left. + B_{\text{SPT}}^{1\text{-loop}} \right] \exp \left[-\frac{k_1^2 + k_2^2 + k_3^2}{12\pi^2} \int dq P_L(q) \right]. \quad (\text{C2})$$